Revision 1

Word count: 8252

TOURMALINE GROWTH IN THE BORDER AND WALL ZONES OF THE EMMONS PEGMATITE (MAINE, USA): EVIDENCE FOR DISEQUILIBRIUM CRYSTALLIZATION AND BOUNDARY LAYER FORMATION

Laura M. van der Does[1*], Niels Hulsbosch[1], Pim Kaskes[2], Jan Elsen[1], Philippe Claeys[2], Philippe Muchez[1] and Mona-Liza C. Sirbescu[3]

[1]KU Leuven, Department of Earth and Environmental Sciences, Celestijnenlaan 200E, 3001 Leuven, Belgium

(*corresponding author: laura.vanderdoes@kuleuven.be)

[2]Vrije Universiteit Brussel, Analytical, Environmental & Geochemistry Research Unit, Department of Chemistry, B-1050 Brussels, Belgium

[3] Central Michigan University, Department of Earth and Atmospheric Sciences, 48859 Mount Pleasant, MI, USA

ABSTRACT

The anisotropic textures, including unidirectional solidification textures and graphic intergrowths, characteristic for pegmatites, are interpreted to result from disequilibrium crystallization at high degrees of undercooling. Experimental studies have revealed the existence of thin boundary layers surrounding the rapidly growing crystals. Here, tourmaline-bearing samples from the outer zones of the Emmons Pegmatite (Maine, USA), are used to examine if a boundary layer can also occur in natural samples. Crystal morphology is linked with geochemistry, to understand the evolution of pegmatite melts and to constrain disequilibrium conditions at large degrees of undercooling. Petrographic studies and semi-quantitative micro-X-ray fluorescence element mapping were conducted to identify crystal morphology and zonation, complemented with electron microprobe analyses to determine major and minor element compositions, and LA-ICP-MS analyses of selected trace elements. Three textural groups were identified: comb-like tourmaline, quartz-tourmaline intergrowths and radiating tourmaline. The intergrowths are optically coherent and are split in three different morphologies: central, second tier and skeletal tourmaline. Most tourmaline is schorl, but chemical variation occurs on three different scales: between textural groups, between different morphologies and intracrystalline. The largest scale geochemical variation is caused by progressive evolution of the melt as it crystallized from the borders inwards, while the intracrystalline variations are attributed to sector zoning. A model is suggested, where the systematic variation of e.g. Mg, Mn and Fe within individual intergrowths is proposed to be the result of crystallization from a boundary layer, rich in water and other fluxing elements (e.g. Li, P, B), formed around the rapidly growing central tourmaline. Here, we show the first examples of boundary layers in natural pegmatites. Furthermore, the results bring into question whether boundary layer tourmaline can be used as a bulk melt indicator in pegmatitic melts.

Keywords: tourmaline, graphic intergrowths, pegmatite, boundary layer, μXRF, EMPA

INTRODUCTION

The most striking characteristic of granitic pegmatites is their extremely coarse (up to tens of meters) grain-size. A wide range of grain-sizes can, however, occur within the pegmatite. Often occurring as dikes, the contact with the host rock, is usually fine-grained, with an inwards coarsening to the core that mostly consists of large, blocky grains (Simmons and Webber 2008;

London 2018). Pegmatite dikes take between a few days up to tens of years to cool completely, depending on their size (Webber et al. 1999; Simmons and Webber 2008; Phelps et al. 2020), challenging the traditional view that large crystals in igneous rocks are always the product of long crystallization and cooling times. Another distinctive characteristic are the anisotropic textures often found in the outer zones of pegmatites (London 2009), including unidirectional solidification textures (UST), with crystals growing directly away from the contact, and graphic intergrowths between different minerals (London 2008, 2018). These textures are assumed to be the result of disequilibrium crystallization (Simmons and Webber 2008). The morphology of growing minerals is controlled mainly by the nucleation and growth rates, and these are controlled by the H_2O content and liquidus undercooling of the melt (Swanson 1977; Nabelek et al. 2010; Sirbescu et al. 2017). Sirbescu and Nabelek (2003) showed that melts far below the granite solidus can exist in the crust, likely due to a high number of fluxing elements such as H_2O, Li, P and B decreasing the crystallization temperatures. Additionally, these elements decrease the viscosity of the melt and the nucleation rate and increase the diffusion rate of elements through the melt (Fenn 1977; Sirbescu and Nabelek 2003; Simmons and Webber 2008). This causes rapid growth of large crystals towards the center of the dike (London 2008), leading to a preferential uptake of previously incompatible elements in the growing crystals. An evolution from euhedral to skeletal morphologies occurs as the degree of undercooling increases (Swanson 1977; Longfellow and Swanson 2011). In experimental studies (London 2005; Sirbescu et al. 2017), and natural studies (Honour et al. 2019), thin boundary layers, with contrasting chemical composition have been observed between rapidly growing crystals and surrounding bulk melt, in particular at low, undercooled temperatures. At these conditions, the high viscosity of the melt prevents the back-diffusion of elements into the bulk melt (London 2014).

In this study, tourmaline from the border and wall zone of the internally zoned Emmons Pegmatite (Maine, USA) is used as a natural laboratory to explore the existence of boundary layers in pegmatites. Tourmaline supergroup minerals are the most common boron rich minerals and are often accessory minerals in igneous, sedimentary, and metamorphic rocks (Henry and Dutrow 1996; London 2016; Bosi 2018). Tourmaline is a complex cyclosilicate with the general formula: $XY_3Z_6[T_6O_8][BO_3]_3V_3W$ where X=Na, Ca, K, □ (vacancy), Y=Li, Mg, Fe^{2+}, Mn^{2+}, Al, Cr^{3+}, V^{3+}, Fe^{3+}, Ti^{4+}, Z=Mg, Al, Fe^{3+}, V^{3+}, Cr^{3+}, T=Si, Al, (B), B=B, V=OH, O, and W=OH, F, O (Hawthorne and Henry 1999). The large chemical variability, combined with large stability range covering most of the crustal P-T conditions, to granulite facies (Henry and Dutrow 1996) and low diffusion of elements through the structure, allows tourmaline to acquire and preserve the chemical signature of its host environment, making it an excellent petrogenetic indicator for the environment in which it grew (Hawthorne and Dirlam 2011; London 2011; van Hinsberg et al. 2011; Dutrow and Henry 2018). Therefore, quartz-tourmaline intergrowth (QTI) textures are ideal candidates for studying the evolution of the pegmatite-forming melts on a micrometer to decimeter scale.

Most researchers accept that pegmatites are the product of either extreme fractional crystallization of granitic magma or anatexis of the crust (London 2005; Simmons et al. 2016). The exact processes responsible for the evolution and crystallization of pegmatite melts are still not completely understood. Jahns and Burnham (1969) proposed a model in which the pegmatitic textures are the result of the coexistence of the pegmatite melt and an exsolved aqueous fluid. Experimental studies on highly evolved compositions by Veksler et al. (2002) and Veksler

(2004) also infer that pegmatite formation involves immiscible/exsolved fluids. They propose that up to three immiscible fluids – a silicate melt, a hydro-saline melt, and an aqueous vapor – can be present during pegmatite formation, which has also been observed in natural rocks (Thomas and Davidson 2016a, 2016b). A contrasting model has been proposed by London (1999, 2005, 2014, 2018) in which pegmatites crystallize from a hydrous, single-phase melt through the process of constitutional zone refining and the creation of boundary layers. As the melt starts to crystallize, incompatible elements pile up at the crystallization front. The boundary layer becomes isolated due to the high viscosity of the melt (London 2014). Due to the pile-up of B, P and F, the boundary layer becomes far more fluxed, enhancing the silicate-H_2O miscibility and causing a lowering of the solidus (London 2005). Because convincing arguments for all models exist, they might all be valid. However, they might be operating at different stages of the crystallization and evolution of the pegmatite.

The aim of this study is to link the tourmaline crystal morphology with variations in its geochemistry, to understand the evolution of the pegmatite melt, and to constrain the disequilibrium crystallization conditions during large liquidus undercooling suggested by the prominent UST and QTI occurrences in the outer zones of the Emmons Pegmatite. This is achieved by detailed petrographic analyses, high-resolution element mapping as well as major, minor and trace element compositions of tourmaline from the border and hanging wall zone of the Emmons Pegmatite.

THE EMMONS PEGMATITE

Located in the Oxford County pegmatite field in western Maine, north-eastern USA (Figure 1), the Emmons pegmatite is a dike intruded into Siluro-Devonian metasedimentary country rock

(Bradley, 1983; Bradley & O'Sullivan, 2017; Solar & Brown, 2001), belonging to the Sebago Migmatite Domain (SMD). The SMD, is mainly composed of pelitic migmatites and diatexites with a few foliated granite intrusions (Solar and Tomascak 2009), and is part of the Central Maine Belt (CMB) in the northern Appalachian Mountains, which stretches from New Brunswick, Canada to Connecticut, USA (Wise and Brown 2010). It is composed of interlayered pelite and psammite rocks, metamorphosed to greenschist and amphibolite facies during the Acadian Orogeny (Solar and Brown 2001). Peak metamorphic conditions occurred at c. 408-404 Ma with temperatures of around 500-520˚C for lower grade metapelitic rocks (Solar et al. 1998; Johnson et al. 2003). U-Pb age determination from apatite and cassiterite yielded ages of 270.4±8.1 Ma and 270-265 Ma, respectively, while ^{40}Ar/^{39}Ar age determinations of muscovite yielded ages of 250.4±2.3 Ma, for the Emmons pegmatite, (Bradley et al., 2016; Felch et al., 2022). In the time gap between peak metamorphic conditions and pegmatite intrusion, the host rock had time to cool to ambient temperatures (Chowdhury et al., 2021 and references therein). In this area, the dominant intrusion is the Sebago Pluton (Wise and Brown 2010), which is 30 Ma older than the pegmatites in the area (Simmons et al. 2018). This age gap and the lack of other potential parental plutons in the vicinity has led to the hypothesis that the Emmons pegmatite is formed by anatexis of the metasedimentary country rock (Simmons et al. 2018; Webber et al. 2019). The contact with the host rock is sharp and no contact metamorphism has occurred because of the intrusion of the pegmatite melt (García-Serrano et al. 2017). The dike is exposed over an area of 120 x 18 meters (Falster et al. 2019).

The Emmons pegmatite is a highly evolved lithium-cesium-tantalum (LCT) pegmatite, moderately enriched in B, Li, Cs and Ta (Falster et al. 2019). The pegmatite is a relatively thin, internally zoned miarolitic dike (Figure 2) that has been historically mined for feldspar. The outermost few centimeters compose the border zone (BZ) that is very fine-grained, mainly composed of feldspars, quartz and micas (García-Serrano et al. 2017) and occasional schorl tourmaline. Inwards, the wall zone (WZ) is about 50-100 cm thick and is much coarser grained. The hanging WZ is characterized by comb-texture schorl perpendicular to the contact (Figure 3) in an assemblage of quartz, feldspar, muscovite, and rare garnet. Typically, the foot WZ has no comb-textures, but instead two well-defined layers of garnet and schorl (García-Serrano et al. 2017; Falster et al. 2019).

The largest volume of the pegmatite is present in the intermediate zone (IZ). This zone is asymmetric, being approx. 50-100 cm above the core and 200-300 cm below the core. The mineral assemblage in the IZ is dominated by graphic intergrowths of quartz and feldspar with subordinate micas and schorl (García-Serrano et al. 2017). The core zone (CZ) is dominated by massive quartz along with feldspar and muscovite. The core zone mineralogy is contrasting from place to place. Exotic Li-, F-, Cs- and Ta-rich minerals occur both in the CZ, and miarolitic cavities on the core margins (Falster et al. 2019). The presence of miarolitic cavities suggests a relatively shallow emplacement depth (García-Serrano et al. 2017; Falster et al. 2019).

The rocks are relatively unaltered and tourmaline occurs in a variety of textures, ranging from elongated, euhedral crystals to skeletal tourmaline intergrown with quartz (QTI; Sirbescu and Hulsbosch 2020). Intergrowths between quartz and tourmaline have been observed before in other pegmatites. Keller et al. (1999) observed “irregular string and radial aggregates forming intergrowths of quartz-tourmaline” in pegmatites from central Namibia. Wadoski et al. (2011) described graphic intergrowths between quartz and tourmaline and noted that they exhibited optical continuity and could be connected in one larger crystal. The intergrowths appear to be forming a "matrix" around larger microcline crystals (Wadoski et al. 2011, p. 387). These both appear to have different characteristics from the intergrowths found in the Emmons Pegmatite.

MATERIALS AND METHODS

FIELD CAMPAIGNS, SAMPLE PREPARATION AND PETROGRAPHY

Tourmaline-bearing samples were collected from the Emmons Pegmatite, during field campaigns in 2012 and 2014. Samples were mainly gathered in situ and from fallen blocks that could be readily correlated with the border and wall zone of the pegmatite. Oriented doubly-polished wafers, 200-300 μm thick, were produced from selected samples and mounted onto glass slides. The QTI samples were too large to fit in one thin section so two QTIs were cut in sequence: QTI A, consisting of thin sections EM06a, EM06a duplicate and EM06b, and QTI B, consisting of thin sections EM9.1-d1 and EM9.1a. During cutting, the aim was to cut the tourmalines parallel to the ***c***-axis. The thin sections were then examined in transmitted light using an Olympus BX40 petrographic microscope at the Department of Earth and Environmental Sciences, KU Leuven, to identify the mineralogy and textures and zoning of tourmaline.

MICRO-X-RAY FLUORESCENCE MAPPING

Micro-X-ray fluorescence (μXRF) element mapping was carried out at the laboratory of the Analytical, Environmental & Geochemistry Research Unit (AMGC) at the Vrije Universiteit Brussel (VUB; Brussels, Belgium) using a Bruker M4 Tornado. Element mapping using μXRF provides a rapid, high-resolution, non-destructive, and cost-efficient method for screening the chemical composition of a range of geological materials (Kaskes et al. 2021), allowing the detection of elements ranging from Na to U with limits of detection for trace elements in the order of 1-10 ppm. A total of nineteen thin sections (200-300 µm thick) were mounted on a plastic holder and mapped during two µXRF mapping runs. Of these runs there were two sets of duplicates (EM06a and EM04b) to allow comparison between the two runs. The µXRF analyses were performed at near-vacuum conditions (20 mbar), using a Rh X-ray source with maximized energy conditions (50 kV, 600 µA), and using two XFlash 430 Silicon Drift detectors. The spatial resolution was 25 µm and acquisition times were 1 ms/pixel for the first run and 5 ms/pixel for the second run. More details on the instrumentation can be found in Kaskes et al. (2021). Two types of element maps were produced: qualitative multi-element maps for screening mineralogical variations, and semi-quantitative single-element heatmaps (Figure 4). The large, motorized stage of the µXRF instrument with a 5 µm step size enables not only a high-resolution visualization of the element distribution within a single thin-section, but also allows direct comparison between multiple thin sections within the same run (Kaskes et al. 2021). These chemical distribution maps were further used to select samples for a more targeted electron microprobe spot analysis campaign.

ELECTRON MICROPROBE ANALYSES

Electron microprobe analyses (EMPA) were carried out to obtain the major and minor element composition of selected tourmaline crystals. These quantitative spot analyses were performed on a JEOL 8200 Superprobe at the University of Copenhagen (UCPH; Copenhagen, Denmark), operating in wavelength-dispersive (WDS) mode. Prior to analysis, all thin sections were carbon coated. Analytical conditions were 15 kV accelerating voltage, 15 nA beam current and a 5 µm spot size. The following standard materials and crystals were used: Si (wollastonite, TAP), Al (corundum, TAP), Mn ($MnTiO_3$, LIF), Fe (hematite, LIF), Ca (wollastonite, PETJ), Ti (rutile, PETJ), V (V_2O_5, LIFH), Cr (Cr_2O_3, LIFH), Na (albite, TAPH), Mg (marjalathi, TAPH) and F (apatite, TAPH). Counting times were 20 seconds on peak and 10 seconds on background for Si, Al, Fe, Ca and Mg, 30 seconds on peak and 15 seconds on background for Mn, Zn, Ti, V and Cr and 16 s on peak and 8 s on background for Na and F. Due to the high concentrations of boron in tourmaline, a fixed value of boron was added to all analyses by atomic ratio with a provisional Si:B ratio of 2:1, for more accurate matrix corrections. In the final data set, however, values derived from stoichiometry, assuming 3 atoms per formula unit (apfu), were used. The structural formulae were calculated using the spreadsheet developed by Julie Selway and Jian Xiong as described in Tindle et al. (2002 and references therein). All Fe was assumed to be Fe^{2+}. Each analysis is an average of 2-5 spots adjacent to each other. In total 642 measurements were performed resulting in 179 analyses across 12 thin sections.

LASER ABLATION INDUCTIVELY COUPLED MASS SPECTROMETRY (LA-ICP-MS)

The tourmaline was analyzed at the GeoRessources Laboratory (Université de Lorraine; Nancy, France). The tourmaline was ablated using an ESI New Wave Research UC193 nm excimer laser using energy frequencies of 5 Hz and 10 Hz and energy densities of 7 J cm^{-2} and 9 J cm^{-2}. The ablated material was carried in a He gas (700 ml/min), mixed with Ar (900 ml/min) before entering the ICP torch. It was subsequently analyzed using an Agilent 7900 quadrupole ICP-MS. The beam size was generally set at 30 µm, but other spot sizes between 20-70 µm were also used. Seven isotopes have been included in this paper (^{7}Li, ^{11}B, ^{39}K, ^{88}Sr, ^{93}Nb, ^{118}Sn, ^{181}Ta), to supplement the EMPA data. Dwell times were 20 ms for all isotopes except Nb, Sn and Ta (30 ms). Standard Reference Material NIST 610 and NIST 612 was used for calibration while SiO_2 concentrations from EMPA was used as an internal standard for each spot.

RESULTS

TOURMALINE FOCUSED PETROGRAPHY

Regardless of its morphology, the tourmaline found in the outer zones of the Emmons Pegmatite, form an unambiguous UST, with the direction of growth roughly aligned perpendicular to the contact with host rock. The diverse morphologies within less than 1 m in the >10 m thick pegmatite dike, suggest that the crystallization conditions changed on a relatively small scale within the pegmatite. Based on textures in hand sample and thin section, three textural groups of tourmaline occur in the border and wall zone of the Emmons pegmatite: comb-like tourmaline, quartz-tourmaline intergrowths (QTIs) and radiating tourmaline (Figure 3). The optical properties of all groups were similar: deep black color in hand samples and optically zoned with pink to purple cores and brown rims, parallel to the *c*-axis, in plane polarized (PPL) transmitted light (Figures 4 and 5). In some case the brown rim did not “cap off” the core at the tip, and the zoning resembles sector zoning (Figure 5). Due to strong pleochroism, the PPL color, in some cases, also varied from deep blue to black, depending on the orientation of the tourmaline cut. In some grains the cut was made parallel, but offset from the *c*-axis, causing only the brown rims to be visible. Additionally, oscillatory, rhombohedral zoning, at an angle relatively to the *c*-axis occur in the cores of larger crystals, while the rims often show a prismatic zonation, parallel to the *c*-axis. Irregular fractures are common, with the tourmaline cores often being the most heavily fractured.

The three textural groups were further subdivided into morphological types. The comb-like tourmaline is composed of numerous tapered prisms (*Type 1*) (Figure 3a) of tourmaline nucleating on the border with the host rock. The crystals flare inwards, thickening in the direction of growth. Generally, the crystals exceed 5 cm in length.

The QTIs, similar to the comb-like tourmaline, are perpendicular to the border but the whole assemblage can reach lengths of up to 50 cm and extends inwards in the wall zone, further than the comb-like tourmaline (Figure 3c). Each QTI is composed of 3 different morphologies of tourmaline (Figure 6). Within a single QTI, tourmaline remains optically coherent, indicating that each QTI can be regarded as a single crystal of tourmaline (Figure 6). The first morphology is the central tourmaline (*Type 2*), forming the root of the QTI. The morphology is usually euhedral to subhedral and elongated in the growth direction. Second tier tourmaline (*Type 3*) occurs as extensions of Type 2. These are still elongated in the growth direction; however, they are much less euhedral and are trending towards a more skeletal morphology. The last morphology of the QTIs, is the skeletal tourmaline (*Type 4*). It occurs mostly as branch-like interconnected grains, but more massive satellite grains also occur (Figure 6). Type 4 tourmaline occurs radially around Types 2 and 3 (Figure 3d). Together, Types 2, 3 and 4 constitute the QTI group.

The least common group is the radiating tourmaline (*Type 5*), located in the pegmatite on the border zone, but in an apophyse of the main dike. Each Type 5 aggregate is composed of several small (<1 cm) elongated subhedral to skeletal grains of tourmaline. As Type 5 is the least common and also not crystallized in the main dike, it will not be discussed in detail in this paper.

Quartz and feldspar dominate the remaining mineral assemblages, with lesser amounts of muscovite, and accessory apatite and garnet. Large (~2 cm) quartz crystals occur directly adjacent to the tourmaline crystals in the comb-like texture. Similar sized feldspar crystals also occur in the samples, but quartz dominates. In the QTIs, the quartz crystals directly adjacent to the tourmaline are usually smaller in size. Around the central tourmaline there is an approximately 1-1.5 mm quartz-dominated ring, before skeletal tourmaline develops (Figure 6).

The only tourmaline appearing here are thin slivers of skeletal tourmaline, perpendicular to the central tourmaline, interstitial between the quartz grains. Most of the quartz involved in the QTI terminate as the tourmalines also terminate, and the larger quartz crystals nucleate further away (Figure 6). The quartz grains within a QTI are not typically in optical continuity, inferring that these are all individual crystals.

ELEMENT MAPPING

The high-resolution µXRF mapping resulted in the detection of a total of 21 elements (Na, Mg, Al, Si, S, K, Ca, Ti, V, Cr, Mn, Fe, Ni, Cu, Zn, Ga, As, Rb, Sr, Y, Zr). Multi-element maps and single-element heatmaps for selected samples are shown in Figure 4, whereas remaining element maps of other samples are found in S1-S33 in Supplementary Material 1. The element mapping revealed significant variations in certain elements among different tourmaline types. The heatmaps for Fe, Mn, and Zn clearly showed increases in concentration from Type 1 to Types 2, 3 and 4 of the QTIs (Figure 4). Furthermore, the Mn values also appear to increase slightly within the QTIs from the central and second tier, Types 2 and 3, to the skeletal, Type 4, tourmaline (Figure 4).

In some QTIs, parts of the interstitial quartz between the skeletal tourmaline appears to be enriched in Zn and Mn as well as Cu and Ni. For Zn and Cu a few of the quartz grains appear more enriched than the adjacent tourmaline. This can potentially be a consequence of Bragg X-ray diffraction peaks yielded by quartz in certain crystallographic orientations, which interfered with the µXRF peaks. The enrichment is concentrated in the quartz between the skeletal tourmaline whereas the Mn enrichment is found closer to the central tourmaline in the QTI.

The optical zoning observed in transmitted light is clearly reflected in the µXRF results, especially in the Ti heatmaps, indicating that the brown rims contain more Ti than the pink-purple cores (Figure 4). The Ca content also shows this variation although more subtle. The Ti heatmaps further highlighted that the fine-grained biotite-, which is part of the foliated host rock found in some border zone samples, is rich in Ti. Contrasting Mn and Fe contents between the brown rims and pink core was also observed in two samples.

The Si and Al heatmaps displayed no intra- or intercrystalline variations in tourmaline. These elements are, however, useful for distinguishing other minerals, such as quartz, plagioclase and muscovite (Figure 4). K is only enriched in muscovite, along with Rb. Y and Zr enrichment occurred mainly in the apatite and small, isolated grains, likely zircon. Mn is strongly enriched in apatite and a few garnets found in the samples.

GEOCHEMICAL CLASSIFICATION OF THE TOURMALINE

The composition of tourmaline in 12 selected samples was analyzed by EMPA. Representative averaged analyses for the tourmaline types are found in Table 1, while all data can be found in Supplementary Material 2. Tourmaline is classified into primary groups based on the X-site occupancy, according to the classification of Henry et al. (2011). The Emmons Pegmatite tourmaline forms a general trend between the alkali groups and the X-vacant group, classifying into the alkali groups, except for two cores that fall into the X-vacant group (Figure 7a). Further classification is based on the Y-site occupancy of Fe^{2+}, Mg and Li, classifying the tourmaline from the alkali group as schorl, with Type 1 having a larger dravite component, and the tourmaline from the X-vacant groups classified as foitite (Figure 7b).

INTERCRYSTALLINE GEOCHEMICAL VARIATION

The most extensive geochemical variation is among the two textural groups. Binary diagrams of Mg, Fe, Zn and Mn clearly show grouping of the comb-like tourmaline (Type 1) and the QTIs (Types 2, 3 and 4) (Figure 8a, b and c). For Zn, there is an overlap between the two groups, however the concentration is significantly lower in the comb-like tourmaline (Figure 8c). Generally, the comb-like tourmaline is characterized by higher Mg and lower Fe, Mn and Zn than the QTIs (Figure 8a-c).

On a smaller scale, a more subtle geochemical variation is also seen among the three types constituting the QTIs. The Mg concentration decreases from Type 2 through Types 3 and 4, with an overlap in the latter (Figure 8a; Table 1). A small group of Type 2 overlaps with Type 4, and these all belong to the same samples. Mn, Fe^{2+} and Zn show an increase from Type 2 through 4. When examining two of the QTIs individually the variation becomes even clearer (Figure 9). Mg decreases from Type 2 to Type 4. Both Mn and Fe^{2+} concentrations increase from Type 2 through 4. Types 3 and 4, overlap in Fe^{2+} for both QTIs, inferring that the concentrations change mostly between Types 2 and 3 and to a lesser extent between Types 3 and 4. The trends are less clear in Zn. In both QTIs the Zn concentrations increase, but with some overlap between Types 2 and 3.

LA-ICP-MS analyses (representative analyses in Table 2 and remaining analyses in Supplementary Material 3) indicate that trace elements K, Li, Sn and Sr show similar trends as the major and minor elements (Figure 10). The Sn content in Type 1 is much lower than in the other types and the Sr concentration is much higher in Type 1 compared to the other types. The K concentration is similar in Types 1 and 2, and then increases to Type 3 and 4. Nb and Ta show very similar trends, when omitting the abnormally high Ta concentrations in sample EM9.2c.

Both concentrations are very low in Type 1 (0.23-0.5 ppm Nb and 0.03-0.05 ppm Ta) and show a gradual increase in Type 2 ($\bar{x}$ = 1.19 ppm Nb and $\bar{x}$ = 0.39 ppm Ta) and Type 3 ($\bar{x}$ = 1.9 ppm Nb and $\bar{x}$ = 0.29 ppm Ta). A relatively large variation in the concentration is seen in Type 4 (0.08-0.76 ppm Ta and 0.56-2.4 ppm Nb), but the average concentration decreases slightly from Type 3 to Type 4 ($\bar{x}$ = 1.5 ppm Nb and $\bar{x}$ = 0.28 ppm Ta).

INTRACRYSTALLINE GEOCHEMICAL VARIATION

On the smallest scale, geochemical variations are also observed within individual grains between the cores and the rims of the grain, regardless of the morphological type. The variations are most pronounced in elements in the X-site; Na, Ca, and X-site vacancy, as well as Ti, which resides in the Y-site (Figure 8). The largest variation is observed in Ti where cores have the lowest values, typically below 0.21 apfu, while rims have values above 0.24 apfu (Figure 8d).

Both Ca and Na are enriched in the rim compared to the cores (Figure 8e). The Ca concentration forms two different trends, since there is also an intercrystalline variation in Ca. The concentration difference between the cores and rims is larger in Type 1 compared to the remaining three types. The rims are enriched in certain trace elements such as Li, K, Nb and Sn.

A more subtle variation between the cores and rims is also observed in Si and Al (Figure 8f), where the cores extend to higher values of both Si and Al, but this variation is less pronounced than the variations seen in the aforementioned elements.

DISCUSSION

CHEMICAL HETEROGENEITY OF THE TOURMALINE

Tourmaline from the border and wall zone of the Emmons Pegmatite varies geochemically on three different scales: (1) among the textural groups, (2) between the pink-purple cores and the brown rims and (3) among the different morphologies of the QTIs. This section only discusses the first two, while the last is discussed in a subsequent section. Furthermore, for elements where there is a significant variation in the core and rim compositions, the rim compositions, corresponding to the "neutral" **a**-sector (van Hinsberg et al. 2006), are used to eliminate the effects of intracrystalline fractionation (Marks et al. 2013).

The largest scale variations between the textural groups (1) are suggested to be caused by an increasing degree of fractionation of the pegmatite melt during crystallization, knowing that the dike crystallized from the border inwards. This was also suggested by García-Serrano et al. (2017), who also studied other Fe-Mg-Mn-bearing minerals in addition to schorl. These authors found that the $\frac{\mathrm{Fe}}{(\mathrm{Fe+Mg})}$ in tourmaline increases from 0.75 to 0.95 from the wall zone inwards, which is consistent with the results from this study (0.66-0.94), indicating a progressive evolution of the melt. In addition, X-vacancy, and Al content (in the Y- and Z-sites) increase while the Ti content decreases from Type 1 to the rest of the tourmaline, further suggesting an increasing degree of evolution from the border inwards (Wadoski et al. 2011; da Costa et al. 2021). The F concentration of the samples shows an increase from Type 1 to the QTIs deeper in the wall zone.

The compositional variation seen between the cores and the rims (2) could be attributed to an evolution of the crystallizing magma adjacent to the crystal, however, the variations fit well with observations from sector zoned tourmalines in both pegmatitic and metamorphic tourmalines (van Hinsberg et al. 2006; van Hinsberg and Schumacher 2007; Marks et al. 2013). The cores, with higher concentration of Al and larger X-vacancy, correspond to the $\boldsymbol{c}^{+}$-sector, while the rims, enriched in Na, Ca, Ti, Fe and Mg, correspond to the ***a***-sector (van Hinsberg and Schumacher 2007; Marks et al. 2013). The transition between cores and rims appears to be sharp (Figure 4). If the variation was caused by a changing composition of the melt adjacent to the crystal, the transition would likely be more gradual, assuming that the crystal grew during one continuous growth event. The latter seems more likely due to the unidirectional nature of the crystals and the inferred fast crystal growth in pegmatites (London 2005). Another observation in favor of sector zoning, is the lack of a "cap" on the core in several samples (Figure 5), where the brown rim does not surround the entire pink core. If the variation was indeed caused by changes in the melt composition, it is expected that the rims would encircle the core fully. Sector zoning occurs as the different sectors of the tourmaline have preferential uptake of certain elements such as Ca and Ti (van Hinsberg et al. 2006; Marks et al. 2013). Metamorphic tourmaline has both a $\boldsymbol{c}^{+}$- and a $\boldsymbol{c}^{-}$-sector, but the latter is not found in the samples studied here. This is likely connected to the unidirectional growth of the tourmaline crystals, which nucleated on a preexisting solid substrate, not permitting the $\boldsymbol{c}^{-}$-sector to grow. Based on this, it is concluded that the intracrystalline variation is most likely caused by sector zoning.

QUARTZ-TOURMALINE INTERGROWTH FORMATION

One of the most striking features of the QTIs are the distinct tourmaline morphologies seen in the individual QTIs. These morphological variations indicate that crystallization conditions must have been different between the three QTI morphology types. The systematic variation within individual QTIs of mainly Mg, Mn, and Zn, and to some extent, Fe^{2+} and F, as well as the trace elements Li, K, Sr and Sn, also indicates that the chemical composition of the crystallizing melt changed. Because the variations happen on millimeter-scale, it is unlikely that these result from compositional changes in the bulk melt, but instead the variations occur on a more local scale. The melt near the contact with the much colder host rock is highly undercooled and viscous (Dingwell et al. 1998; Takeuchi 2011), causing the diffusion of elements through the melt to be very slow. Additionally, several pulses, with all three morphological types in each QTI, are visible as distinct spatial occurrences of the QTIs (Figure 3c) and this would not be expected if the morphological changes were caused by changes in the bulk magma. Another explanation for the QTI growth is therefore needed. It is plausible that factors such as degree of undercooling and the concentration of H_2O and fluxes, controlling nucleation and growth rate (London 1992; Sirbescu et al. 2017), vary locally on a small scale.

Here, we suggest a model that invokes a diffusion-controlled boundary layer around the first formed tourmaline, as a crystallizing melt (Figure 11a). Experimental studies have shown that a boundary layer of incompatible, excluded elements can form around a rapidly growing crystal in a viscous magma (London 1992, 2005; Sirbescu et al. 2017). The high viscosity of the bulk melt prevents back-diffusion, essentially isolating the boundary layer (London 2014).

The boundary layer starts forming around the first growing Type 2 (Figure 11a), the large central tourmaline. Due to the preferential uptake of elements on the different growth planes of the tourmaline, sector zoning is formed (van Hinsberg et al. 2006). Type 2 is the most primitive of the tourmaline in the QTI and preferentially incorporates Mg in the Y-site over less compatible elements including Mn, Zn, Fe^{2+}, K, Li, Sr, Sn, Ta, which instead become concentrated in the boundary layer. As the degree of undercooling decreases and the boundary layer becomes progressively depleted in slowly diffusing B and Al, components required to crystallize tourmaline, the crystallization of Type 2 will halt (London 2008; Nabelek et al. 2010; Dutrow and Henry 2011). As the central tourmaline crystallizes, Si will also become concentrated, and the boundary layer could become oversaturated. As the tourmaline crystallization is halted, quartz nucleates on the border of the central tourmaline, forming a “rim” (approximately 1-1.5 mm) of several quartz grains (Figures 6 and 11b). With progressive quartz crystallization from the boundary layer, tourmaline-forming elements again become concentrated, creating the potential for tourmaline crystallization to restart (Nabelek et al. 2010). An increasing degree of undercooling further adds to this potential as the concentration of B_2O_3 needed to stabilize tourmaline decreases with decreasing temperature (London 2008 and references therein). This is also a possible explanation to the multiple pulses of QTIs (Figure 3b).

At this point, however, the boundary layer is also concentrated in water and fluxing elements, including F, Cl, B and Li (Figure 10b), as these elements are not readily taken up by schorl, and their concentration will therefore increase in the boundary layer. These elements are network modifiers and therefore inhibit the nucleation and crystal growth, but they increase diffusion within the boundary layer (Simmons and Webber 2008). This can lead to supersaturation of the tourmaline components in the boundary layer. An increasing degree of supersaturation in the boundary layer as well as space competition with co-crystallizing quartz grains, influences the morphology changes observed from Type 2 through 4. The higher the degree of supersaturation, the more the crystals will move towards a skeletal habit (Longfellow and Swanson 2011).

Eventually nucleation and crystal growth occur, but due to the low nucleation rate and high diffusion, tourmaline grows as very coarse crystals. As nucleation and crystal growth commences, tourmaline and quartz are in competition for space. This concurrent and competitive crystallization of tourmaline and quartz generates the graphic texture associated with Type 3 and 4 tourmaline (Figure 11c), similar to what has been suggested for graphic intergrowths of feldspar and quartz in pegmatites (Fenn 1986; Sirbescu et al. 2017; Baker et al. 2018). Although

Types 3 and 4 show an overlap in many elements, slight geochemical variation can be observed (Figure 9), indicating that the chemical composition of the boundary layer continues to evolve slightly between the crystallization of Types 3 and 4, with increasing distance from the central tourmaline. The intermediate nature, both in geochemistry and morphology of Type 3 infers that it crystallized before Type 4. This can occur when the longitudinal growth is faster than the transverse growth. In QTI B, the rim of the quartz crystal also appears around Type 3, indicating that it crystallized before the tourmaline crystallization halted and the quartz nucleated on it (Figure 6).

The ring of quartz around the central tourmaline and the presence of only quartz directly adjacent to the tourmaline (Figure 6) can be seen as a consequence of a silica-saturated boundary layer. Si is very slow to diffuse, compared to other elements in the boundary layer (Acosta-Vigil et al. 2006). As other elements, such as alkalis diffuse rapidly to sustain crystallization of e.g., coeval feldspars and micas, the Si oversaturation in the boundary layer increases even further.

CRYSTALLIZATION TEMPERATURES OF THE TOURMALINE

As the nucleation delay took place in the boundary layer, due to higher concentrations of water and other fluxing elements, the temperature of the boundary layer could decrease, in turn increasing the degree of undercooling. A higher degree of undercooling is inferred by the skeletal morphology of Type 4 tourmaline (Swanson 1977; Longfellow and Swanson 2011). Here, the intersector tourmaline thermometer proposed by van Hinsberg & Schumacher (2007) is used to assess temperature changes between tourmaline types. Their geothermometer has been calibrated using metamorphic tourmaline and is based on the intersector partitioning of elements, which is most pronounced in Ca and Ti. From the EMPA data, core-rim pairs were chosen from within the same grain, where the core represents the $\boldsymbol{c}^{+}$- sector and the rim the ***a***-sector (Fig. 6). In some cases, the same core analysis was matched with different rim analyses from the same grain, simply because more rim than core analyses were acquired. There is a higher number of core-rim pairs in Types 1 and 2 (n=46 and n=81, respectively) than Types 3 and 4 (n=6 and n=13, respectively), primarily because the grains of Types 3 and 4 are smaller and therefore were not always cut directly through the middle of the *c*-axis to display both cores and rims.

Rim to core ratios were calculated for Ca and Ti (see Supplementary Material 4). Around one fourth and half of the ratios, respectively, were higher than the calibration of van Hinsberg & Schumacher (2007). For the ratios that overlapped with the calibration, temperatures were read from their graph, yielding temperatures spanning 337˚C-597˚C for the Ti ratios and 343˚C-600˚C for the Ca ratios (Figure 12). The temperature ranges derived from the two elements overlap, however the overall trend between the tourmaline types, does not fully agree (Figure 12). This could be related to uncertainties in the calibration data or the fact that Ti is mainly controlled by the polar surface charge, while Ca could also be influenced by differences in X-site exposure (van Hinsberg and Schumacher 2007) or simply because fewer temperatures could be determined from Ca. For these reasons, only the Ti temperatures are discussed further. Temperatures of all tourmaline types fall under the haplogranitic liquidus, inferring that all tourmaline crystallized at undercooled conditions (Figure 12a). Type 1 tourmaline crystallized at lower temperatures than Type 2 tourmaline, corresponding to a higher degree of undercooling for Type 1. This is expected since Type 1 occurs right at the border of the pegmatite, where the melt likely cooled more rapidly upon emplacement of the pegmatite melt. Within the QTIs a trend of decreasing temperature occurs from Type 2 through Types 3 and 4 (Figure 12a). This variation was also observed in temperatures derived from FIs in the Emmons pegmatite, where the central, Type 2 tourmaline, had average temperatures of 405˚C, while the temperature decreased to 340˚C in the skeletal, Type 4 tourmaline (Yoder et al. 2021). This indicates that the skeletal tourmaline (Type 4) in the QTIs most likely crystallized under higher degrees of undercooling than the central tourmaline (Type 2). However, care must be taken when making conclusions based on the tourmaline thermometer. Firstly, the geothermometer was calibrated using metamorphic tourmaline (van Hinsberg and Schumacher 2007), likely under equilibrium conditions, whereas the tourmaline studied in this paper crystallized under disequilibrium conditions. Secondly, the temperature variation within the QTIs is >200˚C, which is quite a large variation within a distance of a few millimeters. Lastly, only few temperatures for Types 3 and 4 could be calculated, making the trend less robust.

IMPLICATIONS

The results presented here provide the first examples of boundary layers forming in natural pegmatites. The geochemical and morphological variations observed over a short distance, within the pegmatite, indicate that the crystallization conditions can change rapidly in the pegmatitic melt. This implies that local, disequilibrium processes may play an important role in the overall formation of pegmatites. The geochemical variation in major, minor and trace elements on several scales brings into question whether trace elements in boundary layer tourmaline can be used as a bulk melt indicator in pegmatites. Current studies focus on the role an aqueous fluid might play in the boundary layer.

ACKNOWLEDGEMENTS

This research is funded by the KU Leuven in the form of a PhD scholarship for Laura M. van der Does. Pim Kaskes is supported by a Research Foundation Flanders (FWO) PhD Fellowship (11E6621N). Philippe Claeys acknowledges the support of the FWO Hercules program for the purchase of the µXRF instrument and that of the VUB Strategic Research Program. The authors thank Tod Waight (University of Copenhagen) for assistance with electron microprobe analyses as well as useful comments and discussion for creating a protocol for analyzing the tourmaline. Marie-Christine Boiron and Chantal Peiffert (Université de Lorraine, CNRS) are thanked for their support with the LA-ICP-MS analyses. Herman Nijs is thanked for the preparation of the thin sections used for analyses. Jan Elsen, Niels Hulsbosch and Philippe Muchez are members of the KU Leuven Institute for Sustainable Metals and Minerals.

REFERENCES

Acosta-Vigil, A., London, D., Morgan, G.B., and Dewers, T.A. (2006) Dissolution of Quartz, Albite, and Orthoclase in H2O-Saturated Haplogranitic Melt at 800°C and 200 MPa: Diffusive Transport Properties of Granitic Melts at Crustal Anatectic Conditions. Journal of Petrology, 47, 231–254.

Baker, D.R., Sirbescu, M.-L., Maneta, V., Webber, K.L., and Simmons, W.B. (2018) Quantitative Analysis of Natural and Experimental Graphic Textures. The Canadian Mineralogist, 56, 625–643.

Bosi, F. (2018) Tourmaline crystal chemistry. American Mineralogist, 103, 298–306.

Bradley, D., Shea, E., Buchwaldt, R., Bowring, S., Benowitz, J., O'Sullivan, P., and McCauley, A. (2016) Geochronology and Tectonic Context of Lithium-Cesium-Tantalum Pegmatites in the Appalachians. The Canadian Mineralogist, 54, 945–969.

Bradley, D.C. (1983) Tectonics of the Acadian Orogeny in New England and Adjacent Canada. Journal of Geology, 91, 381–400.

Bradley, D.C., and O'Sullivan, P. (2017) Detrital zircon geochronology of pre- and syncollisional strata, Acadian orogen, Maine Appalachians. Basin Research, 29, 571–590.

Chowdhury, P., Chakraborty, S., and Gerya, T. V. (2021) Time will tell: Secular change in metamorphic timescales and the tectonic implications. Gondwana Research, 93, 291–310.

da Costa, I.R., Antunes, I.M.H.R., and Récio, C. (2021) The Mg/(Fe + Mg) ratio and the Ti and A site contents of tourmaline as promising indicators of granitic magma evolution. Journal of Iberian Geology, 47, 307–321.

Dingwell, D.B., Hess, K.U., and Romano, C. (1998) Viscosity data for hydrous peraluminous granitic melts: Comparison with a metaluminous model. American Mineralogist, 83, 236–239.

Dutrow, B.L., and Henry, D.J. (2011) Tourmaline: A geologic DVD. Elements, 7, 301–306.

——— (2018) Tourmaline compositions and textures: Reflections of the fluid phase. Journal of Geosciences, 63, 99–110.

Falster, A.U., Simmons, W.B., Webber, K.L., Dallaire, D.A., Nizamoff, J.W., and Sprague, R.A. (2019) The Emmons Pegmatite, Greenwood, Oxford County, Maine. Rocks and Minerals, 94, 498–519.

Felch, M., Eusden Jr., J., Bradley, D., Koteas, C., Whittaker, A.H., Marvinney, R., Holm-Denoma, C., Pianowski, L.S., Smith, S.M., Kinney, S., and others (2022) Geologic Mapping and Exploration for Li-bearing Pegmatites of the Rumford Series in the Oxford County Pegmatite Field, ME, USA. Geological Society of America Abstracts with Programs, 54, 257–5.

Fenn, P.M. (1977) The Nucleation and Growth of Alkali Feldspars from Hydrous Melts. The Canadian Mineralogist, 15, 135–161.

——— (1986) On the origin of graphic granite. American Mineralogist, 71, 325–330.

García-Serrano, J., Roda-Robles, E., Villaseca, C., and Simmons, W. (2017) Fe-Mn-(Mg) distribution in primary phosphates and silicates, and implications for the internal evolution of the Emmons rare-element pegmatite (Maine, USA). NGF Abstracts and Proceedings, 2, 37–40.

Hanson, S.L., Falster, A.U., Simmons, W.B.S., Sprague, R., Vignola, P., Rotiroti, N., Andó, S., and Hatert, F. (2018) Tantalowodginite, (Mn0.5 0.5)TaTa2O8, a New Mineral Species from the Emmons Pegmatite, Uncle Tom Mountain, Maine, U.S.A. The Canadian Mineralogist, 56, 543–553.

Hawthorne, F.C., and Dirlam, D.M. (2011) Tourmaline the Indicator Mineral: From Atomic Arrangement to Viking Navigation. Elements, 7, 307–312.

Hawthorne, F.C., and Henry, D.J. (1999) Classification of the minerals of the tourmaline group. European Journal of Mineralogy, 11, 201–216.

Henry, D.J., and Dutrow, B.L. (1996) Metamorphic Tourmaline and its Petrologic Applications. In E.S. Grew and L.M. Anovitz, Eds., Boron: Mineralogy, Petrology and Geochemistry pp. 275–279.

Henry, D.J., Novák, M., Hawthorne, F.C., Ertl, A., Dutrow, B.L., Uher, P., and Pezzotta, F. (2011) Nomenclature of the tourmaline-supergroup minerals. American Mineralogist, 96, 895–913.

Honour, V.C., Holness, M.B., Charlier, B., Piazolo, S.C., Namur, O., Prosa, T.J., Martin, I., Helz, R.T., Maclennan, J., and Jean, M.M. (2019) Compositional boundary layers trigger liquid unmixing in a basaltic crystal mush. Nature Communications, 10, 1–8.

Jahns, R.H., and Burnham, C.W. (1969) Experimental Studies of Pegmatite Genesis: I. A model for the Derivation and Crystallization of Granitic Pegmatites. Economic Geology, 64, 843–864.

Johnson, T.E., Brown, M., and Solar, G.S. (2003) Low-pressure subsolidus and suprasolidus phase equilibria in the MnNCKFMASH system: Constraints on conditions of regional metamorphism in western Maine, northern Appalachians. American Mineralogist, 88, 624–638.

Kaskes, P., Déhais, T., de Graaff, S.J., Goderis, S., and Claeys, P. (2021) Micro–X-ray fluorescence (µXRF) analysis of proximal impactites: High-resolution element mapping, digital image analysis, and quantifications. In W.U. Reimold and C. Koeberl, Eds., Large Meteorite Impacts and Planetary Evolution VI: Geological Society of America Special Paper Vol. 550, pp. 171–206.

Keller, P., Roda Robles, E., Pesquera Pérez, A., and Fontan, F. (1999) Chemistry, paragenesis and significance of tourmaline in pegmatites of the Southern Tin Belt, central Namibia. Chemical Geology, 158, 203–225.

London, D. (1992) The Application of Experimental Petrology to the Genesis and Crystallization of Granitic Pegmatites. The Canadian Mineralogist, 30, 499–540.

——— (1999) Melt Boundary-Layers and the Growth of Pegmatitic Textures. The Canadian Mineralogist, 37, 826–827.

——— (2005) Granitic pegmatites: An assessment of current concepts and directions for the future. Lithos, 80, 281–303.

——— (2008) Pegmatites, 347 p. The Canadian Mineralogist Special Publication Vol. 10.

——— (2009) The Origin of Primary Textures in Granitic Pegmatites. The Canadian Mineralogist, 47, 697–724.

——— (2011) Experimental Synthesis and Stability of Tourmaline: A Historical Overview. The Canadian Mineralogist, 49, 117–136.

——— (2014) A petrologic assessment of internal zonation in granitic pegmatites. Lithos, 184–187, 74–104.

——— (2016) Reading Pegmatites-Part 2: What Tourmaline Says. Rocks and Minerals, 91, 132–149.

——— (2018) Ore-forming processes within granitic pegmatites. Ore Geology Reviews, 101, 349–383.

Longfellow, K.M., and Swanson, S.E. (2011) Skeletal Tourmaline, Undercooling, and Crystallization History of the Stone Mountain Granite, Georgia, U.S.A. The Canadian Mineralogist, 49, 341–357.

Marks, M.A.W., Marschall, H.R., Schühle, P., Guth, A., Wenzel, T., Jacob, D.E., Barth, M., and Markl, G. (2013) Trace element systematics of tourmaline in pegmatitic and hydrothermal systems from the Variscan Schwarzwald (Germany): The importance of major element composition, sector zoning, and fluid or melt composition. Chemical Geology, 344, 73–90.

Nabelek, P.I., Whittington, A.G., and Sirbescu, M.-L.C. (2010) The role of H2O in rapid emplacement and crystallization of granite pegmatites: Resolving the paradox of large crystals in highly undercooled melts. Contributions to Mineralogy and Petrology, 160, 313–325.

Phelps, P.R., Lee, C.T.A., and Morton, D.M. (2020) Episodes of fast crystal growth in pegmatites. Nature Communications, 11, 1–10.

Robinson, P., Tucker, R.D., Bradley, D., Berry, H.N., and Osberg, P.H. (1998) Paleozoic orogens in New England, USA. GFF, 120, 119–148.

Simmons, W.B., and Webber, K.L. (2008) Pegmatite genesis: state of the art. European Journal of Mineralogy, 20, 421–438.

Simmons, W.B., Falster, A., Webber, K., Roda-Robles, E., Boudreaux, A.P., Grassi, L.R., and Freeman, G. (2016) Bulk composition of Mt. Mica Pegmatite, Maine, USA: Implications for the Origin of an LCT Type Pegmatite by Anatexis. The Canadian Mineralogist, 54, 1053–1070.

Simmons, W.B., Webber, K., Falster, A., and Roda-Robles, E. (2018) Post-Orogenic, Pre-Rifting Anatectic Origin of the Oxford Co., Maine USA Pegmatite Field. International Mineralogical Association Abstract Volume, 288.

Sirbescu, M.-L.C., and Hulsbosch, N. (2020) Inclusion trapping during disequilibrium pegmatite crystallization: lessons from tourmaline-quartz intergrowths. Goldschmidt2020 Abstract, 2403–2403.

Sirbescu, M.-L.C., and Nabelek, P.I. (2003) Crustal melts below 400 °C. Geology, 31, 685–688.

Sirbescu, M.-L.C., Schmidt, C., Veksler, I. V., Whittington, A.G., and Wilke, M. (2017) Experimental Crystallization of Undercooled Felsic Liquids: Generation of Pegmatitic Texture. Journal of Petrology, 58, 539–568.

Solar, G.S., and Brown, M. (2001) Petrogenesis of Migmatites in Maine, USA: Possible Source of Peraluminous Leucogranite in Plutons? Journal of Petrology, 42, 789–823.

Solar, G.S., and Tomascak, P.B. (2009) The Sebago Pluton and the Sebago Migmatite Domain, southern Maine: Results from New Studies. 2009 Annual Meeting of the Northeastern Section of the Geological Society of America, Field Trip, 1–24.

Solar, G.S., Pressley, R.A., Brown, M., and Tucker, R.D. (1998) Granite ascent in convergent orogenic belts: Testing a model. Geology, 26, 711–714.

Swanson, S.E. (1977) Relation of nucleation and crystal-growth rate to the development of granitic textures. American Mineralogist, 62, 966–978.

Takeuchi, S. (2011) Preeruptive magma viscosity: An important measure of magma eruptibility. Journal of Geophysical Research: Solid Earth, 116.

Thomas, R., and Davidson, P. (2016a) Origin of miarolitic pegmatites in the Königshain granite/Lusatia. Lithos, 260, 225–241.

——— (2016b) Revisiting complete miscibility between silicate melts and hydrous fluids, and the extreme enrichment of some elements in the supercritical state - Consequences for the formation of pegmatites and ore deposits. Ore Geology Reviews, 72, 1088–1101.

Tindle, A.G., Breaks, F.W., and Selway, J.B. (2002) Tourmaline in petalite-subtype granitic pegmatites: Evidence of fractionation and contamination from the Pakeagama Lake and Separation Lake areas of northwestern Ontario, Canada. The Canadian Mineralogist, 40, 753–788.

van Hinsberg, V.J., and Schumacher, J.C. (2007) Intersector element partitioning in tourmaline: a potentially powerful single crystal thermometer. Contributions to Mineralogy and Petrology, 153, 289–301.

van Hinsberg, V.J., Schumacher, J.C., Kearns, S., Mason, P.R.D., and Franz, G. (2006) Hourglass sector zoning in metamorphic tourmaline and resultant major and trace-element fractionation. American Mineralogist, 91, 717–728.

van Hinsberg, V.J., Henry, D.J., and Marschall, H.R. (2011) Tourmaline: An Ideal Indicator of its Host Environment. The Canadian Mineralogist, 49, 1–16.

Veksler, I., Thomas, R., and Schmidt, C. (2002) Experimental evidence of three coexisting immiscible fluids in synthetic granitic pegmatite. American Mineralogist, 87, 775–779.

Veksler, I. V. (2004) Liquid immiscibility and its role at the magmatic-hydrothermal transition: a summary of experimental studies. Chemical Geology, 210, 7–31.

Wadoski, E.R., Grew, E.S., and Yates, M.G. (2011) Compositional evolution of tourmaline-supergroup minerals from granitic pegmatites in the Larsemann hills, East Antarctica. The Canadian Mineralogist, 49, 381–405.

Webber, K.L., Simmons, W.B., Falster, A.U., and Foord, E.E. (1999) Cooling rates and crystallization dynamics of shallow level pegmatite-aplite dikes, San Diego County, California. American Mineralogist, 84, 708–717.

Webber, K.L., Simmons, W.B., Falster, A.U., and Hanson, S.L. (2019) Anatectic Pegmatites of the Oxford County Pegmatite Field, Maine, USA. The Canadian Mineralogist, 57, 811–815.

Wise, M.A., and Brown, C.D. (2010) Mineral chemistry, petrology and geochemistry of the Sebago granite-pegmatite system, Southern Maine, USA. Journal of Geosciences, 55, 3–26.

Yoder, E., Sirbescu, M., Brennan, C., and Hulsbosch, N. (2021) Crystallization of an Internally-Zoned Granitic Pegmatite: Insights From Fluid and Melt Inclusions, Emmons Pegmatite, Oxford County, Maine. Geological Society of America Abstracts with Programs, 53.

Figure 1. Simplified geological map showing metamorphic zones, structures, and major plutons in Maine (ME), northeastern USA. Yellow rectangle indicates the location of the Oxford County Pegmatite field with the Emmons Pegmatite marked by the yellow star. CMB: Central Maine Belt, S: Sebago Pluton (modified from (Solar and Tomascak (2009) and Robinson et al. (1998).

Figure 2. Schematic cross-section of the Emmons Pegmatite showing the internal zonation and asymmetry of the dike. The red, dashed rectangle indicates the sampling location (modified from Hanson et al. (2018)).

Figure 3. The three different textural tourmaline groups that occur in the BZ and WZ of the Emmons Pegmatite. The comb texture directly on the contact with the metamorphic host rock (**a**), the radiating tourmaline (**b**) and the QTIs both parallel to the ***c***-axis (**c**) and perpendicular to the ***c***-axis (**d**). Notice in **c** the multiple pulses of QTI assemblages and in **d** how the skeletal tourmaline fully surrounds the central tourmaline. Arrows indicate the direction of growth.

Figure 4. µXRF multi-element maps of Si, Fe, Ca and Rb and selected semi-quantitative, single-element heatmaps for representative samples the two main textural groups: comb-like tourmaline (EM04b duplicate) and quartz-tourmaline intergrowth (EM06a duplicate). The arrows indicate the growth direction for each sample. The µXRF maps are derived from the run with acquisition time 5 ms/pixel and the color scale is the same for each element, allowing semi-quantitative comparison between the samples. Pl: plagioclase, Tur: tourmaline, Qz: quartz, Ms: muscovite, Ap: apatite.

Figure 5. Photos showing the lack of a rim "cap" at the tip of the tourmaline grains in Types 2, 3 (**a**) and 4 (**b**, **c**) tourmaline in sample EM9.1-d1 and in Type 2 in sample EM06a (**d**). The cores are assumed to correspond to the $\boldsymbol{c}^+$-sector while the rims correspond to the ***a***-sector. The $\boldsymbol{c}^-$-sector is not seen in these grains due to the highly directional growth.

Figure 6. Photomicrograph of sample EM9.1-d1 in plane polarized light (**a**) and cross polarized light (**b**) showing the three types of tourmaline occurring in the quartz-tourmaline intergrowths. The green dashed line shows the front of quartz, nucleating on the first formed central tourmaline (Type 2) (**a**). From the cross polarized ligth micrograph (**b**) it is evident that all tourmaline in the QTI are in optical continuity. Furthermore, the size and shape of the quartz crystals is better visualized.

Figure 7. Ternary diagrams for the classification of tourmaline based on Henry et al. (2011), using the Emmons Pegmatite EMPA data from this study (n=797). The two samples that classify into the X-vacant group on a have a yellow border on **b**, and are foitite instead of schorl. Srl: Schorl, Drv: Dravite, Elb: Elbaite.

Figure 8. Binary diagrams for the chemical composition in atoms per formula unit of the different types of Emmons Pegmatite tourmaline (n=642).

Figure 9. Boxplots showing the systematic variation in atoms per formula unit in the two QTIs that were studied. Small black crosses show the data points for each box and whiskers. Black dots are outliers.

Figure 10. Boxplots of selected trace elements showing the variations between tourmaline types. All concentrations are in ppm. In the Sr plot the range for Type 1 is excluded for better visualization of the Sr concentration in the other types. An outlier at 1.8 ppm in Type 4 is also excluded. Small black crosses show the data points for each box and whiskers. Black dots are outliers.

Figure 11. Schematic representation of the evolution of formational processes of the quartz-tourmaline intergrowths (QTIs) at the Emmons Pegmatite. **a**) The central tourmaline grows rapidly, forming a boundary layer of excluded, incompatible elements. **b**) The boundary layer becomes undersaturated in tourmaline components and crystallization of tourmaline stops. Quartz nucleates on the tourmaline surface and starts to grow. **c**) The boundary layer becomes progressively saturated in tourmaline components, but the high concentation of H_2O (± Li, B, F and P) inhibits nucleation and growth of tourmaline, causing higher degrees of undercooling and supersaturation. Eventually, coarse grains of tourmaline will crystallize, competing with quartz

and forming the QTIs. For simplicity, individual quartz grains have not been drawn in the intergrowths. Tur2: Type 2 tourmaline, Tur3: Type 3 tourmaline, Tur4: Type 4 tourmaline, BL: boundary layer, Fsp: feldspar, Qz: quartz

Figure 12. Estimated crystallization temperatures of the different tourmaline types. Temperatures are calculated based on intersector variations in Ti (**a**) and Ca (**b**) in the tourmaline (van Hinsberg and Schumacher 2007). Less data points are available for Types 3 and 4, because less core-rim pairs were available.

Table 1. Representative EMPA data for each tourmaline type and in each zone.

Type	Type 1		Type 2		Type 3		Type 4	
Sample	EM04b†		EM06a		EM06a		EM9.1-d1	
Zone	Core	Rim	Core	Rim	Core	Rim	Core	Rim
wt%								
SiO_2	35.79 ± 0.10	35.22 ± 0.29	34.95 ± 0.20	34.60 ± 0.21	35.07 ± 0.14	34.84 ± 0.18	35.14 ± 0.18	34.74 ± 0.17
TiO_2	0.10 ± 0.01	0.33 ± 0.02	0.13 ± 0.02	0.33 ± 0.03	0.11 ± 0.02	0.31 ± 0.02	0.13 ± 0.02	0.33 ± 0.02
Al_2O_3	35.00 ± 0.06	34.22 ± 0.12	34.48 ± 0.15	33.97 ± 0.07	34.19 ± 0.24	34.05 ± 0.24	34.61 ± 0.15	33.58 ± 0.14
FeO	11.32 ± 0.12	11.12 ± 0.18	13.75 ± 0.12	13.48 ± 0.14	13.92 ± 0.15	13.52 ± 0.19	13.79 ± 0.08	13.93 ± 0.2
MgO	2.23 ± 0.09	2.62 ± 0.10	1.16 ± 0.01	1.44 ± 0.01	1.01 ± 0.05	1.12 ± 0.03	0.87 ± 0.02	0.99 ± 0.04
CaO	0.09 ± 0.01	0.24 ± 0.30	0.05 ± 0.01	0.12 ± 0.01	0.04 ± 0.02	0.10 ± 0.01	0.03 ± 0.01	0.09 ± 0.02
Na_2O	1.69 ± 0.04	2.02 ± 0.05	1.68 ± 0.05	2.02 ± 0.02	1.69 ± 0.06	1.94 ± 0.04	1.66 ± 0.03	1.95 ± 0.06
MnO	0.14 ± 0.03	0.12 ± 0.02	0.21 ± 0.03	0.21 ± 0.03	0.21 ± 0.03	0.21 ± 0.03	0.25 ± 0.03	0.25 ± 0.03
ZnO	0.09 ± 0.03	0.08 ± 0.05	0.17 ± 0.05	0.14 ± 0.06	0.17 ± 0.05	0.21 ± 0.05	0.18 ± 0.03	0.18 ± 0.03
V_2O_3	bdl	bdl	bdl	0.010 ± 0.012	bdl	0.004 ± 0.008	0.007 ± 0.009	0.004 ± 0.008
Cr_2O_3	0.005 ± 0.006	0.006 ± 0.012	0.007 ± 0.009	bdl	bdl	bdl	bdl	0.01 ± 0.01

F	bdl	0.10 ± 0.11	0.19 ± 0.02	0.16 ± 0.06	0.18 ± 0.03	0.21 ± 0.05	0.13 ± 0.05	0.23 ± 0.02
B_2O_3*	10.56 ± 0.03	10.47 ± 0.06	10.39 ± 0.05	10.35 ± 0.03	10.37 ± 0.03	10.37 ± 0.04	10.42 ± 0.04	10.30 ± 0.04
LiO_2*	0.26 ± 0.02	0.30 ± 0.04	0.12 ± 0.02	0.19 ± 0.01	0.15 ± 0.04	0.23 ± 0.03	0.17 ± 0.01	0.22 ± 0.03
Total	100.9	100.4	100.7	100.5	100.6	100.6	100.9	100.3
apfu								
Si	5.89 ± 0.01	5.84 ± 0.03	5.84 ± 0.01	5.81 ± 0.02	5.88 ± 0.01	5.84 ± 0.02	5.86 ± 0.02	5.86 ± 0.01
Ti	0.012 ± 0.001	0.042 ± 0.002	0.016 ± 0.002	0.042 ± 0.003	0.014 ± 0.003	0.039 ± 0.003	0.016 ± 0.002	0.041 ± 0.01
Al (T)	0.11 ± 0.01	0.16 ± 0.03	0.16 ± 0.01	0.19 ± 0.02	0.12 ± 0.01	0.16 ± 0.02	0.14 ± 0.02	0.14 ± 0.01
Al (Z)	6.00 ± 0.00	6.00 ± 0.00	6.00 ± 0.00	6.00 ± 0.00	6.00 ± 0.00	6.00 ± 0.00	6.00 ± 0.00	6.00 ± 0.00
Al (Y)	0.68 ± 0.01	0.54 ± 0.02	0.64 ± 0.01	0.53 ± 0.01	0.63 ± 0.03	0.57 ± 0.03	0.67 ± 0.01	0.53 ± 0.02
Fe^{2+}	1.56 ± 0.02	1.54 ± 0.03	1.92 ± 0.02	1.89 ± 0.01	1.95 ± 0.02	1.90 ± 0.03	1.92 ± 0.01	1.97 ± 0.03
Mg	0.55 ± 0.02	0.65 ± 0.02	0.29 ± 0.00	0.36 ± 0.00	0.25 ± 0.01	0.28 ± 0.01	0.22 ± 0.01	0.25 ± 0.01
Ca	0.017 ± 0.001	0.043 ± 0.005	0.008 ± 0.001	0.022 ± 0.002	0.008 ± 0.003	0.018 ± 0.001	0.005 ± 0.002	0.016 ± 0.004
Na	0.54 ± 0.01	0.65 ± 0.01	0.55 ± 0.02	0.66 ± 0.01	0.55 ± 0.02	0.63 ± 0.01	0.54 ± 0.01	0.64 ± 0.02
Mn	0.02 ± 0.00	0.02 ± 0.00	0.03 ± 0.00	0.03 ± 0.00	0.03 ± 0.00	0.03 ± 0.00	0.04 ± 0.00	0.04 ± 0.00

Zn	0.01 ± 0.00	0.01 ± 0.01	0.02 ± 0.01	0.02 ± 0.01	0.02 ± 0.01	0.03 ± 0.01	0.02 ± 0.00	0.02 ± 0.01
V	bdl	bdl	bdl	0.00 ± 0.00	bdl	0.00 ± 0.00	0.00 ± 0.00	0.00 ± 0.00
Cr	0.00 ± 0.00	0.00 ± 0.00	0.00 ± 0.00	bdl	bdl	bdl	Bdl	0.00 ± 0.00
F	bdl	0.05 ± 0.06	0.10 ± 0.01	0.08 ± 0.03	0.10 ± 0.01	0.11 ± 0.03	0.07 ± 0.03	0.12 ± 0.01
B*	3.00 ± 0.00	3.00 ± 0.00	3.00 ± 0.00	3.00 ± 0.00	3.00 ± 0.00	3.00 ± 0.00	3.00 ± 0.00	3.00 ± 0.00
Li*	0.17 ± 0.02	0.20 ± 0.03	0.08 ± 0.01	0.13 ±0.01	0.10 ± 0.03	0.16 ± 0.02	0.11 ± 0.01	0.15 ± 0.02
vac.	0.44 ± 0.01	0.31 ± 0.01	0.45 ± 0.02	0.32 ± 0.03	0.44 ± 0.02	0.35 ± 0.01	0.46 ± 0.01	0.34 ± 0.02

Notes: * Not measured directly, calculated values. †Duplicate of sample EM04b. bdl: below detection limit. Numbers after ± indicate standard deviation. Apfu is calculated using the spreadsheet developed by Julie Selway and Jian Xiong (Tindle et al. 2002).

Table 2. Representative LA-ICP-MS data for each tourmaline type and in each zone.

Type	Type 1		Type 2†	Type 3		Type 4	
Sample	EM04c-1	EM04b	EM9.1-d1	EM06a	EM9.1-d1	EM9.1a	EM9.1-d1
Zone	Core	Rim	Core	Core	Rim	Core	Rim
ppm							
^{7}Li	68.42	69.24	91.88	238.42	240.41	436.30	468.43
^{11}B	24292	26835	27740	28351	27199	29520	27181
^{39}K	217.88	339.50	279.82	283.77	398.04	299.75	323.83
^{88}Sr	0.62	1.67	0.14	0.05	0.26	0.1	0.1
^{93}Nb	0.24	0.67	0.67	0.95	1.58	1.62	1.78
^{118}Sn	8.82	24.06	24.06	30.33	37.52	43.87	47.89
^{181}Ta	0.04	0.17	0.17	0.31	0.27	0.19	0.22

Notes: †No rim analyses exsist for Type 2. bdl: below detection limit.

Figure 1

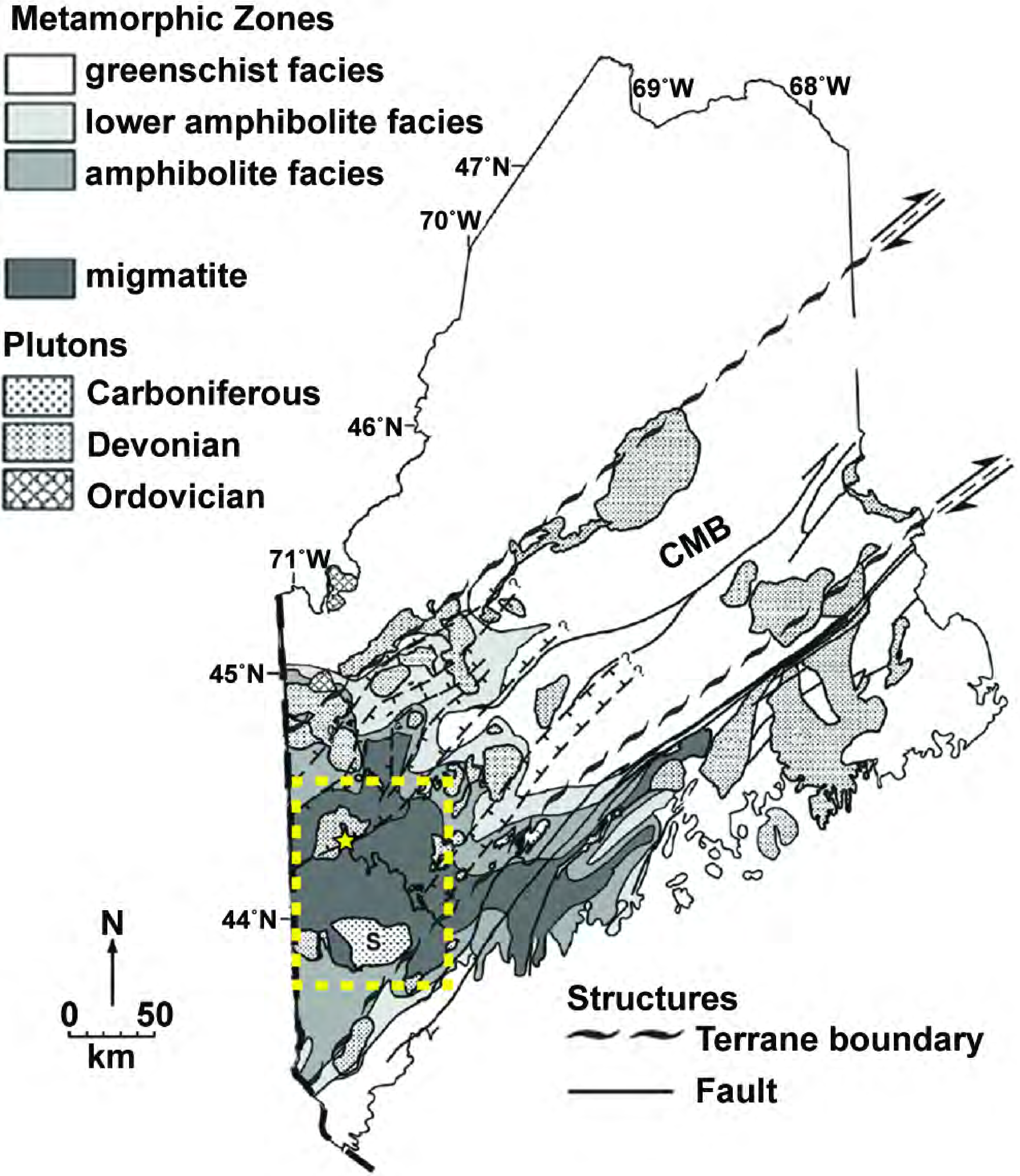
Metamorphic Zones
greenschist facies
lower amphibolite facies
amphibolite facies
migmatite
Plutons
Carboniferous
Devonian
Ordovician
69°W
68°W
47°N
70°W
46°N
71°W
45°N
44°N
CMB
S
N
0
50
km
Structures
Terrane boundary
Fault

Figure 2

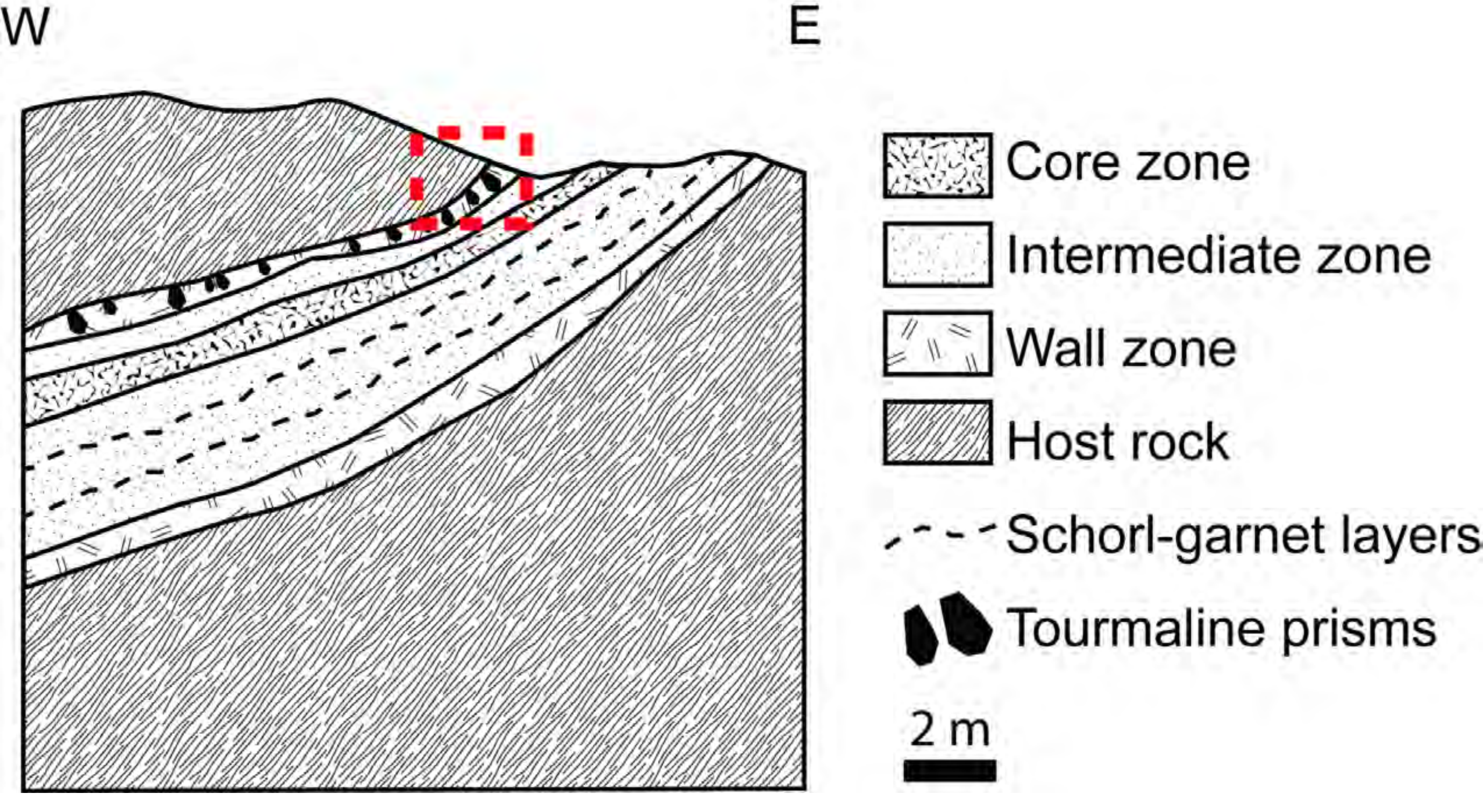
W
E
Core zone
Intermediate zone
Wall zone
Host rock
Schorl-garnet layers
Tourmaline prisms
2 m

Figure 3

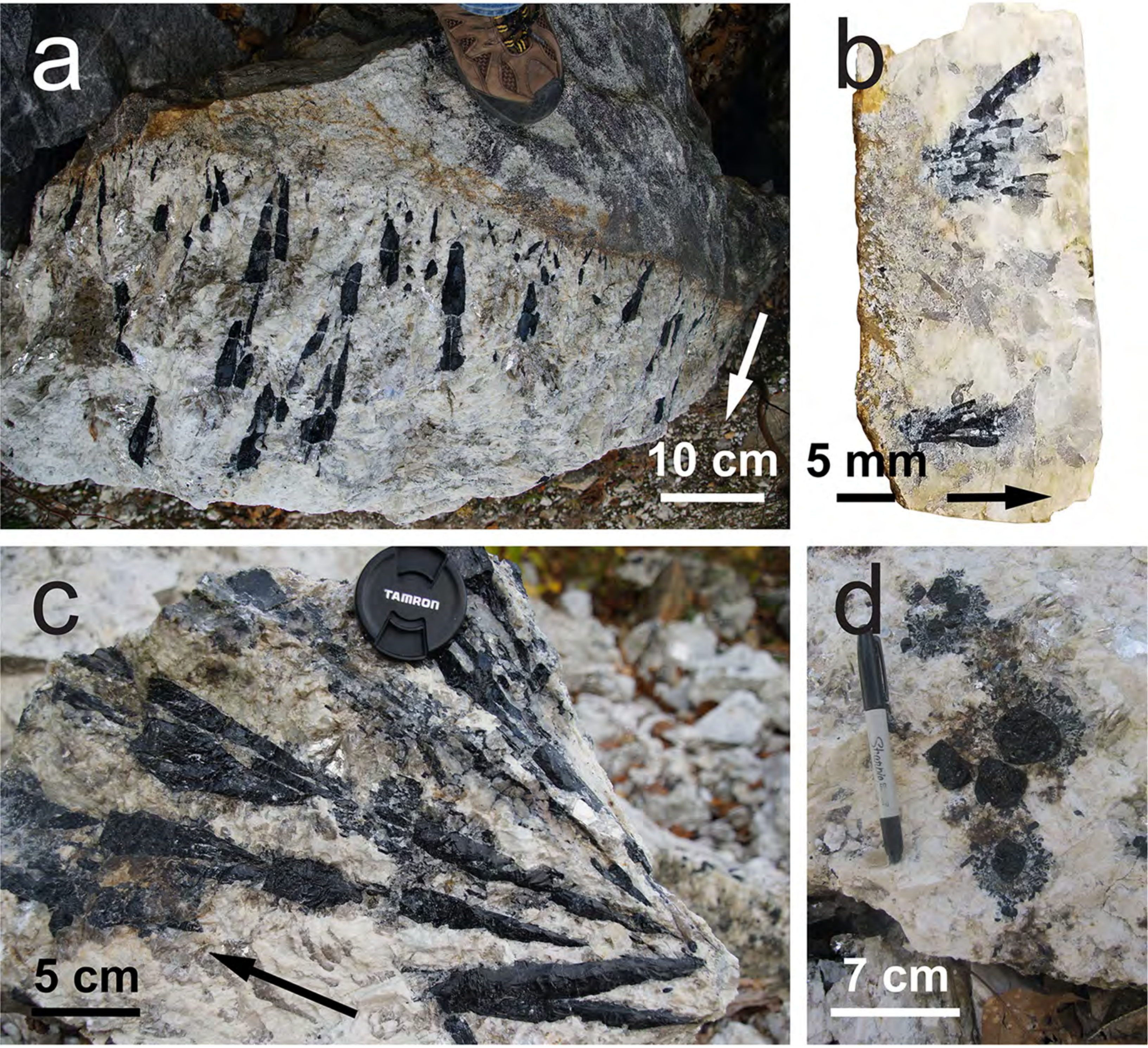

Figure 4

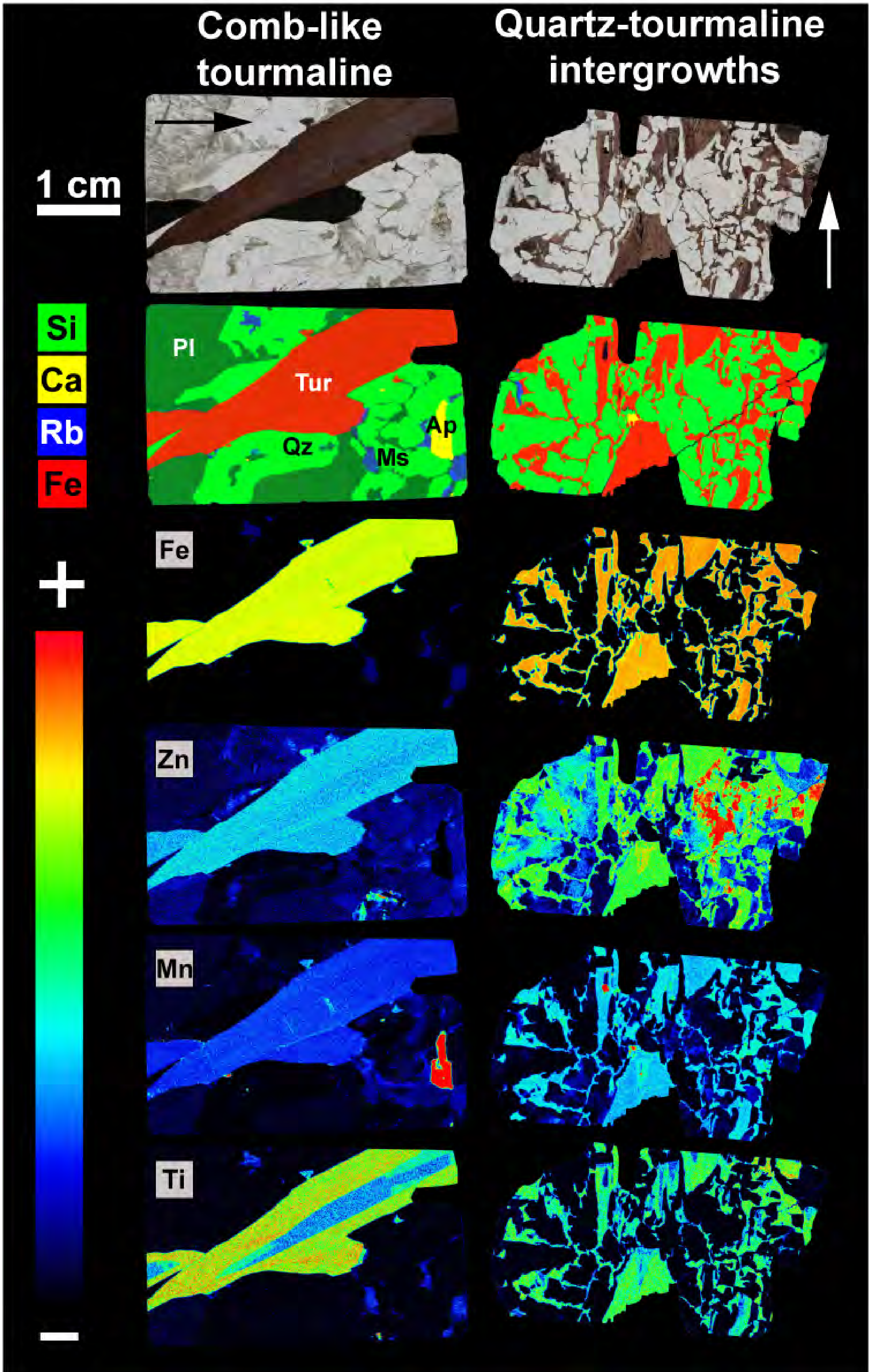
Comb-like tourmaline
Quartz-tourmaline intergrowths
1 cm
Si
Ca
Rb
Fe
Pl
Tur
Qz
Ms
Ap
Fe
Zn
Mn
Ti
+
–

Figure 5

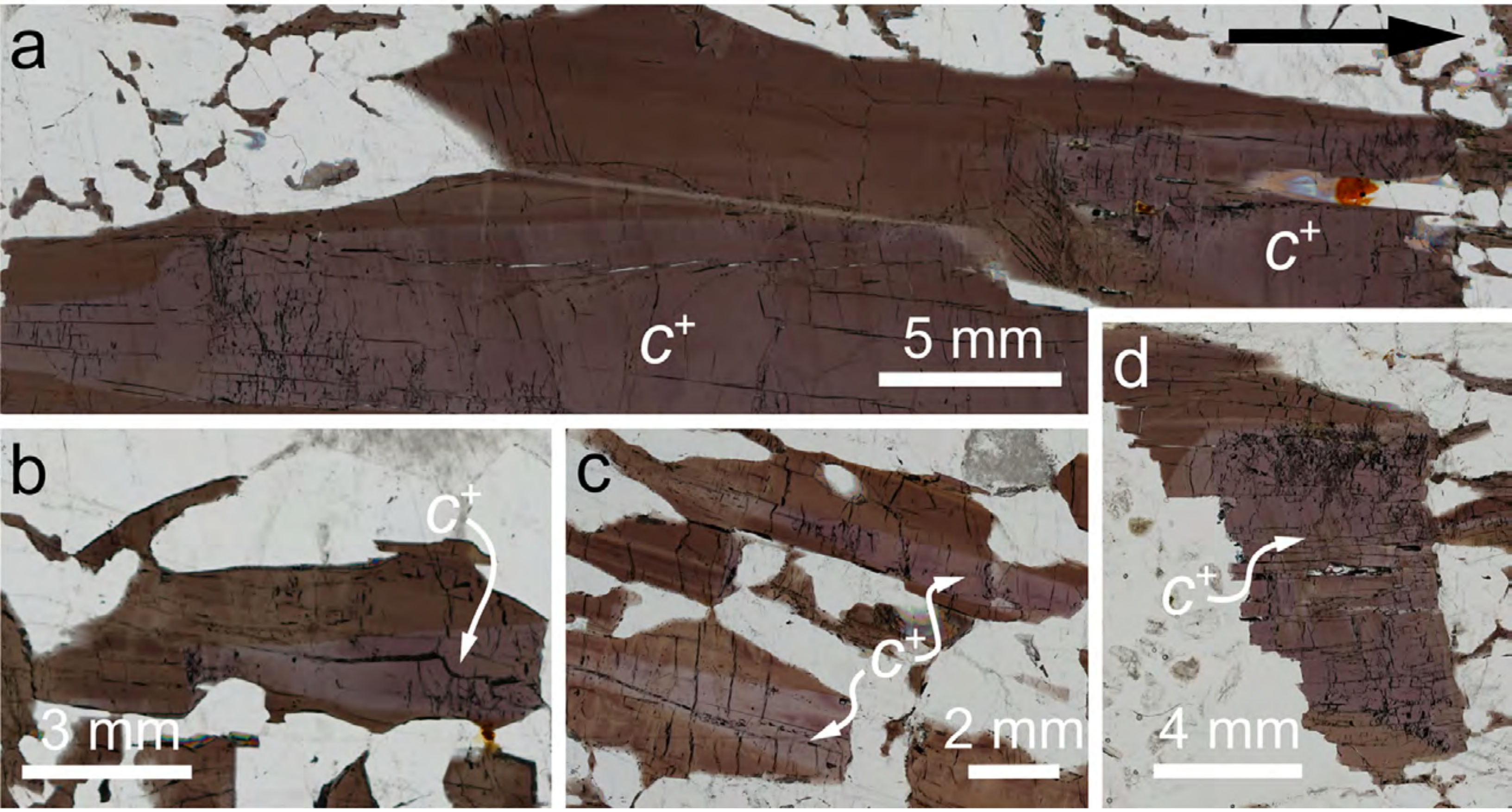

Figure 6

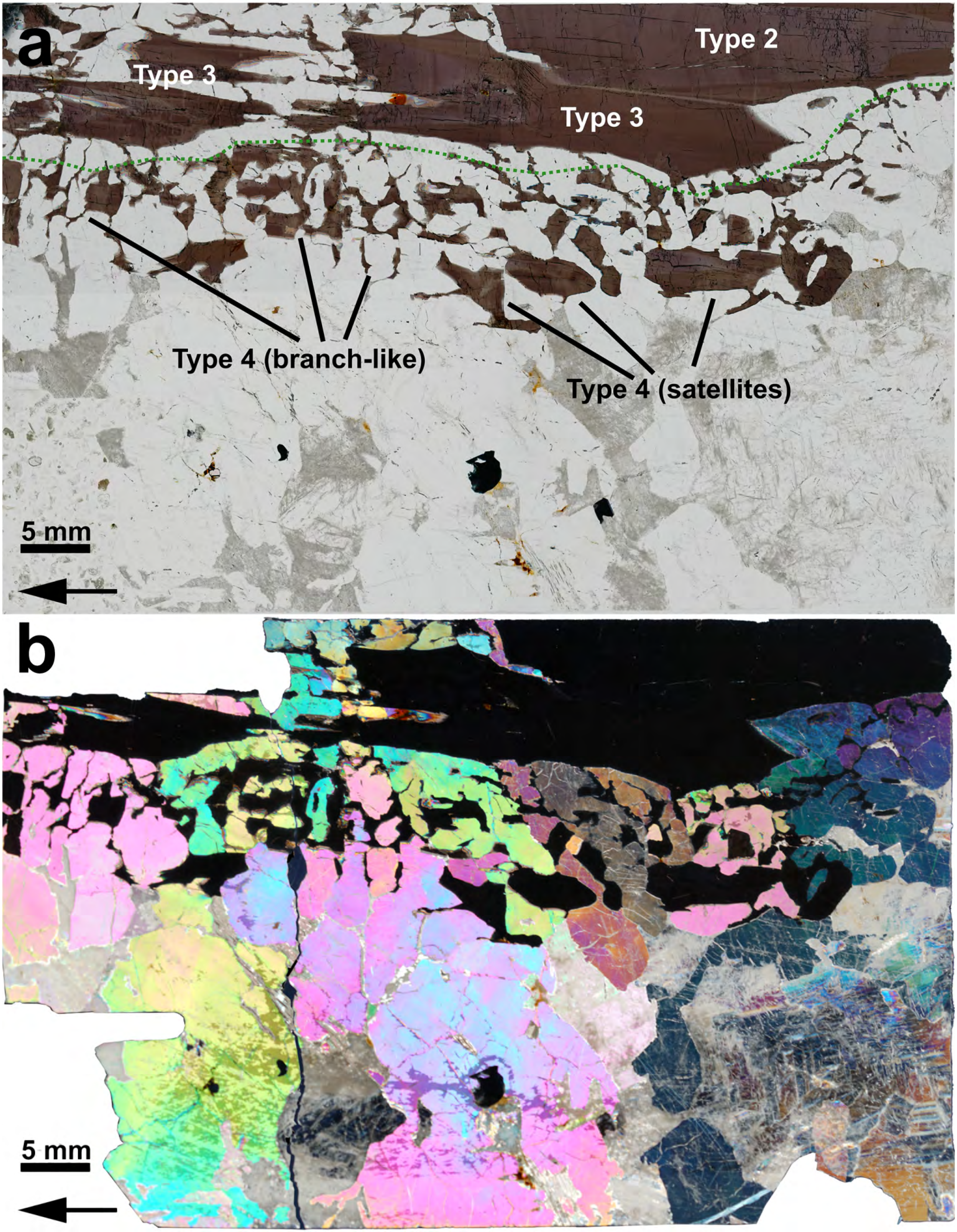
a
Type 3
Type 2
Type 3
Type 4 (branch-like)
Type 4 (satellites)
5 mm
b
5 mm

Figure 7

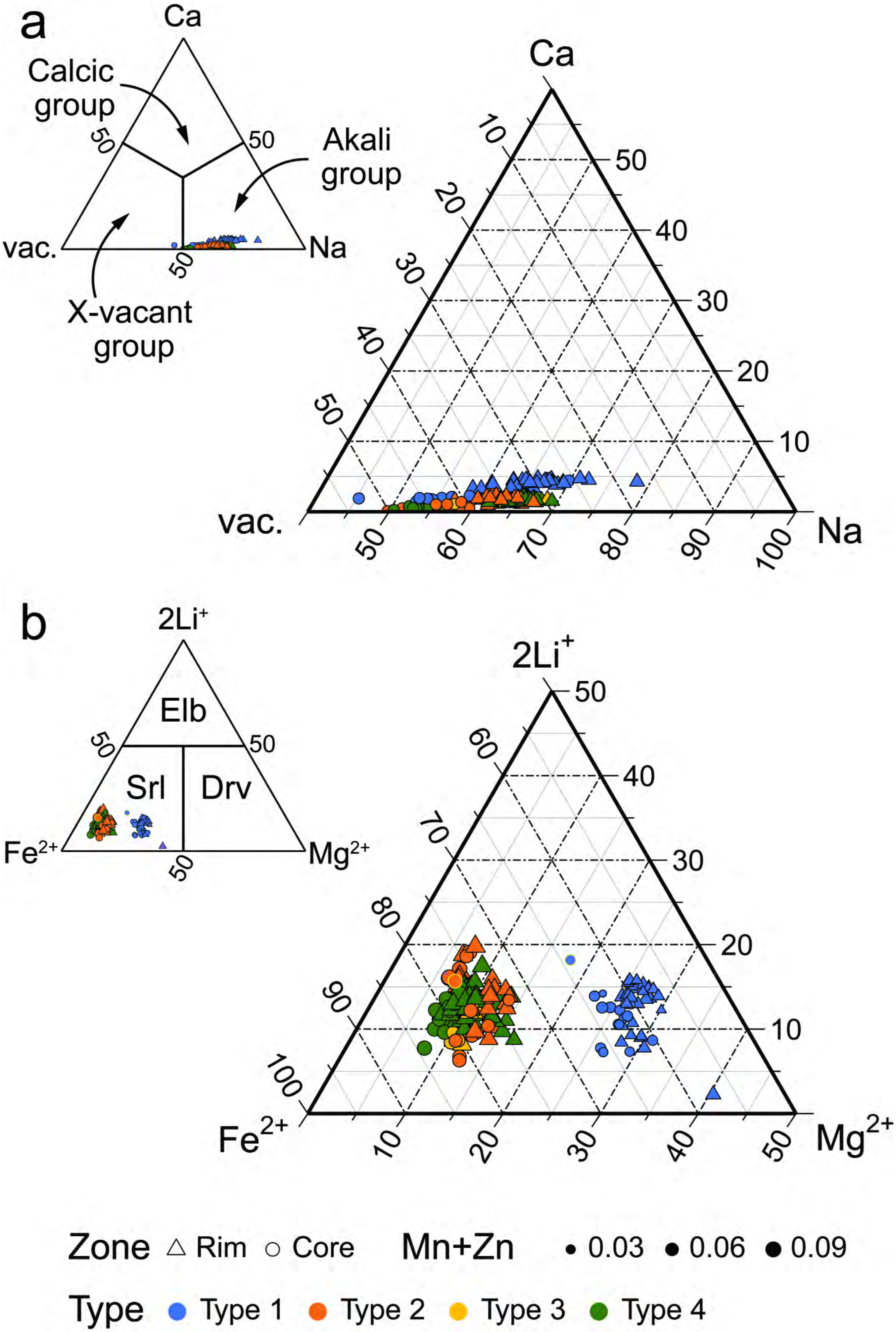
a
Ca
Calcic group
Akali group
X-vacant group
vac.
Na
50
50
50
Ca
10
20
30
40
50
50
40
30
20
10
vac.
Na
50
60
70
80
90
100
b
2Li⁺
Elb
Srl
Drv
Fe²⁺
Mg²⁺
50
50
50
2Li⁺
50
40
30
20
10
60
70
80
90
100
Fe²⁺
Mg²⁺
10
20
30
40
50
Zone △ Rim ○ Core
Mn+Zn ● 0.03 ● 0.06 ● 0.09
Type ● Type 1 ● Type 2 ● Type 3 ● Type 4

Figure 8

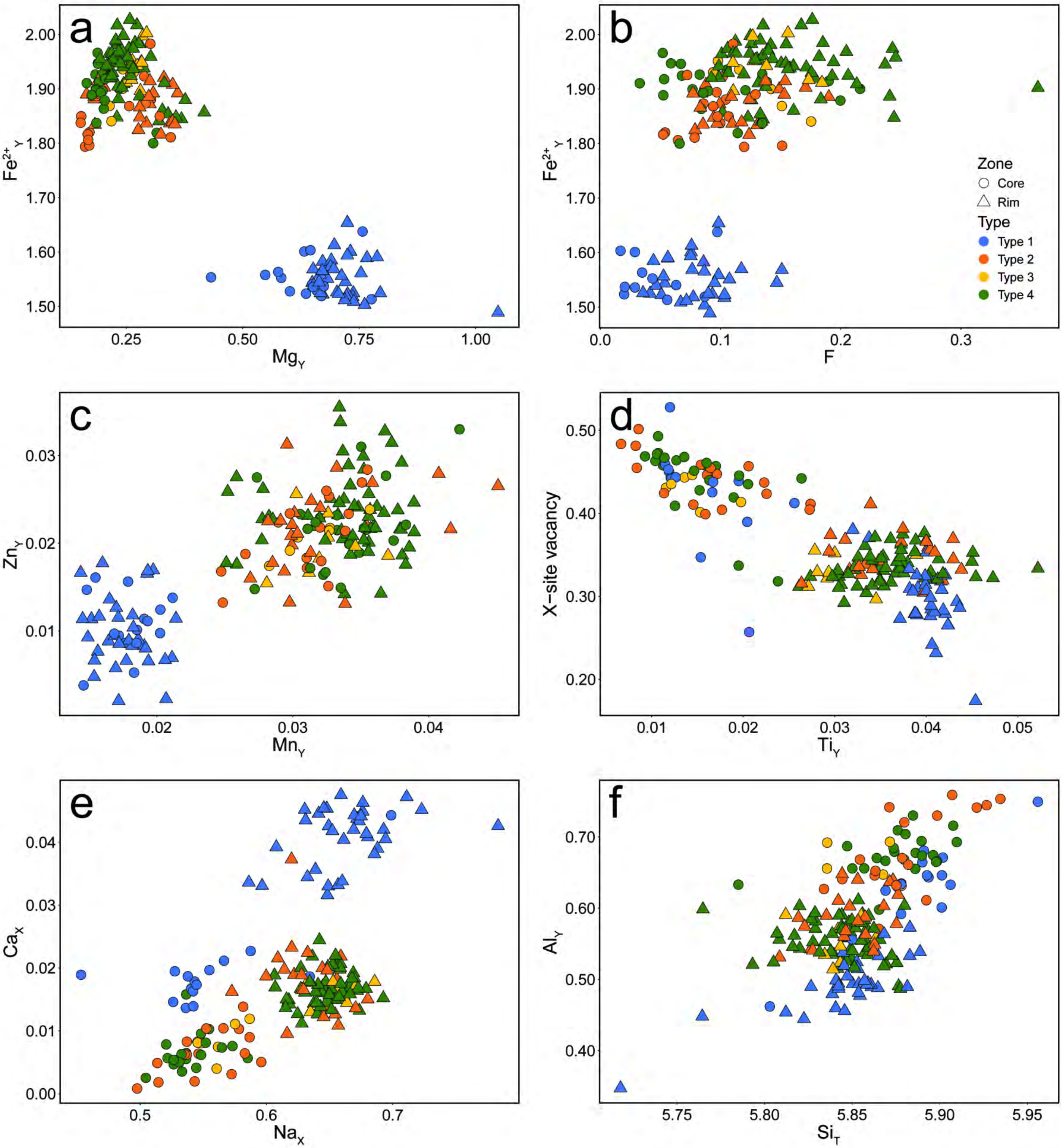
a
Fe^{2+}_Y
2.00
1.90
1.80
1.70
1.60
1.50
0.25
0.50
0.75
1.00
Mg_Y
b
Fe^{2+}_Y
0.0
0.1
0.2
0.3
F
Zone
○ Core
△ Rim
Type
● Type 1
● Type 2
● Type 3
● Type 4
c
Zn_Y
0.03
0.02
0.01
0.02
0.03
0.04
Mn_Y
d
X−site vacancy
0.50
0.40
0.30
0.20
0.01
0.02
0.03
0.04
0.05
Ti_Y
e
Ca_X
0.04
0.03
0.02
0.01
0.00
0.5
0.6
0.7
Na_X
f
Al_Y
0.70
0.60
0.50
0.40
5.75
5.80
5.85
5.90
5.95
Si_T

Figure 9

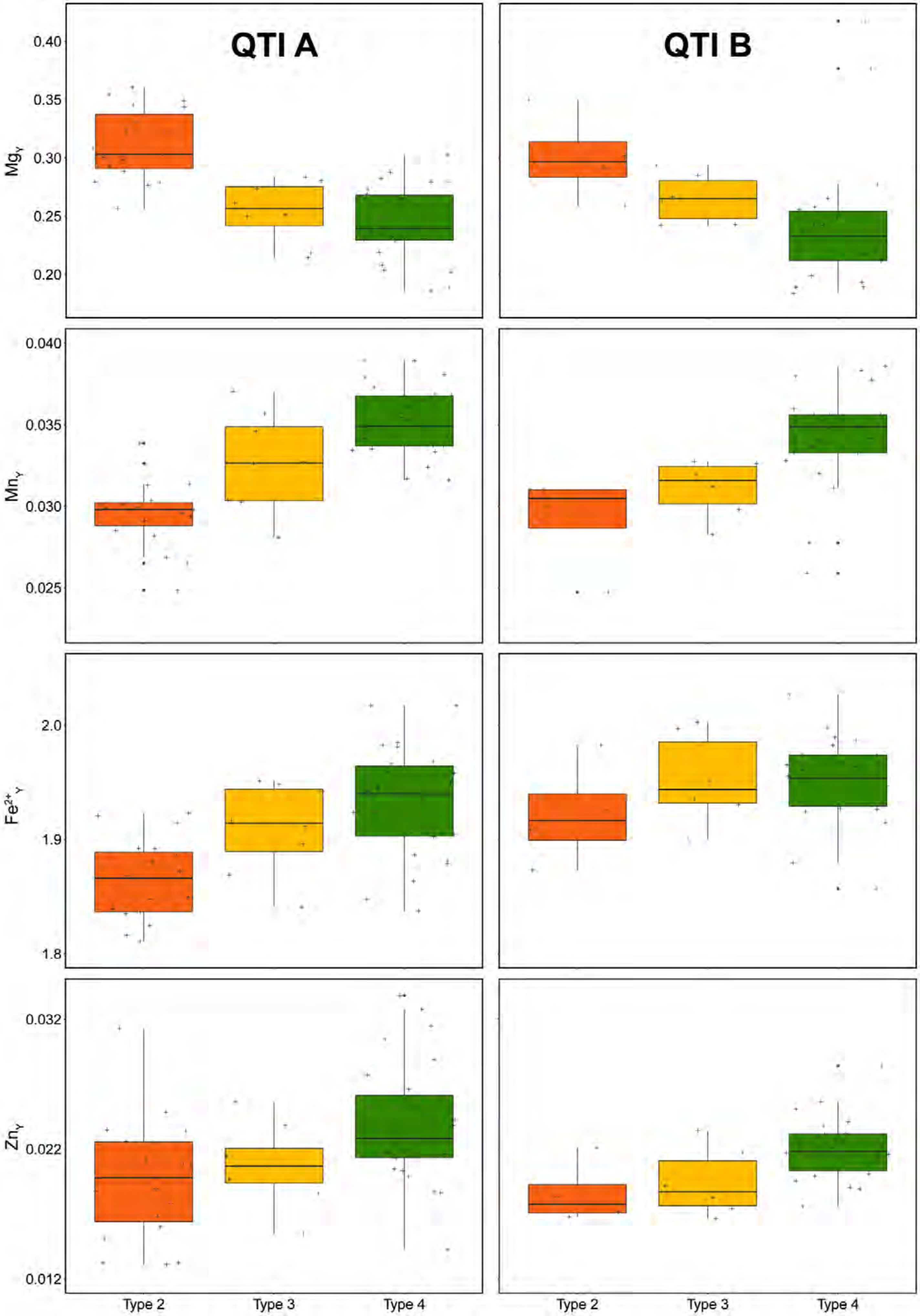
QTI A
QTI B
Mg$_Y$
0.40
0.35
0.30
0.25
0.20
Mn$_Y$
0.040
0.035
0.030
0.025
Fe$^{2+}_Y$
2.0
1.9
1.8
Zn$_Y$
0.032
0.022
0.012
Type 2
Type 3
Type 4
Type 2
Type 3
Type 4

Figure 10

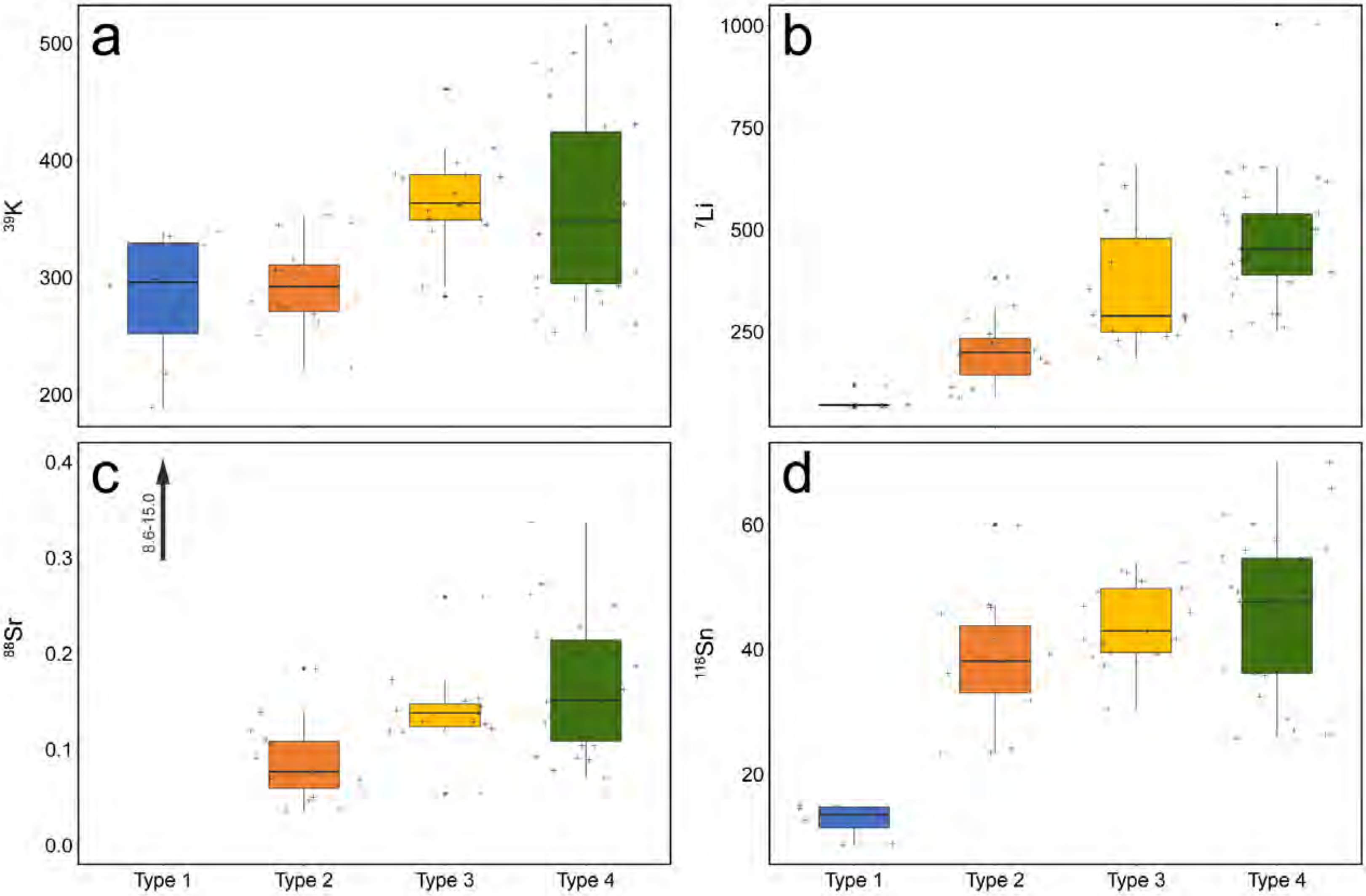
a
500
400
300
200
39K
b
1000
750
500
250
7Li
c
0.4
0.3
0.2
0.1
0.0
88Sr
8.6-15.0
d
60
40
20
118Sn
Type 1
Type 2
Type 3
Type 4
Type 1
Type 2
Type 3
Type 4

Figure 11

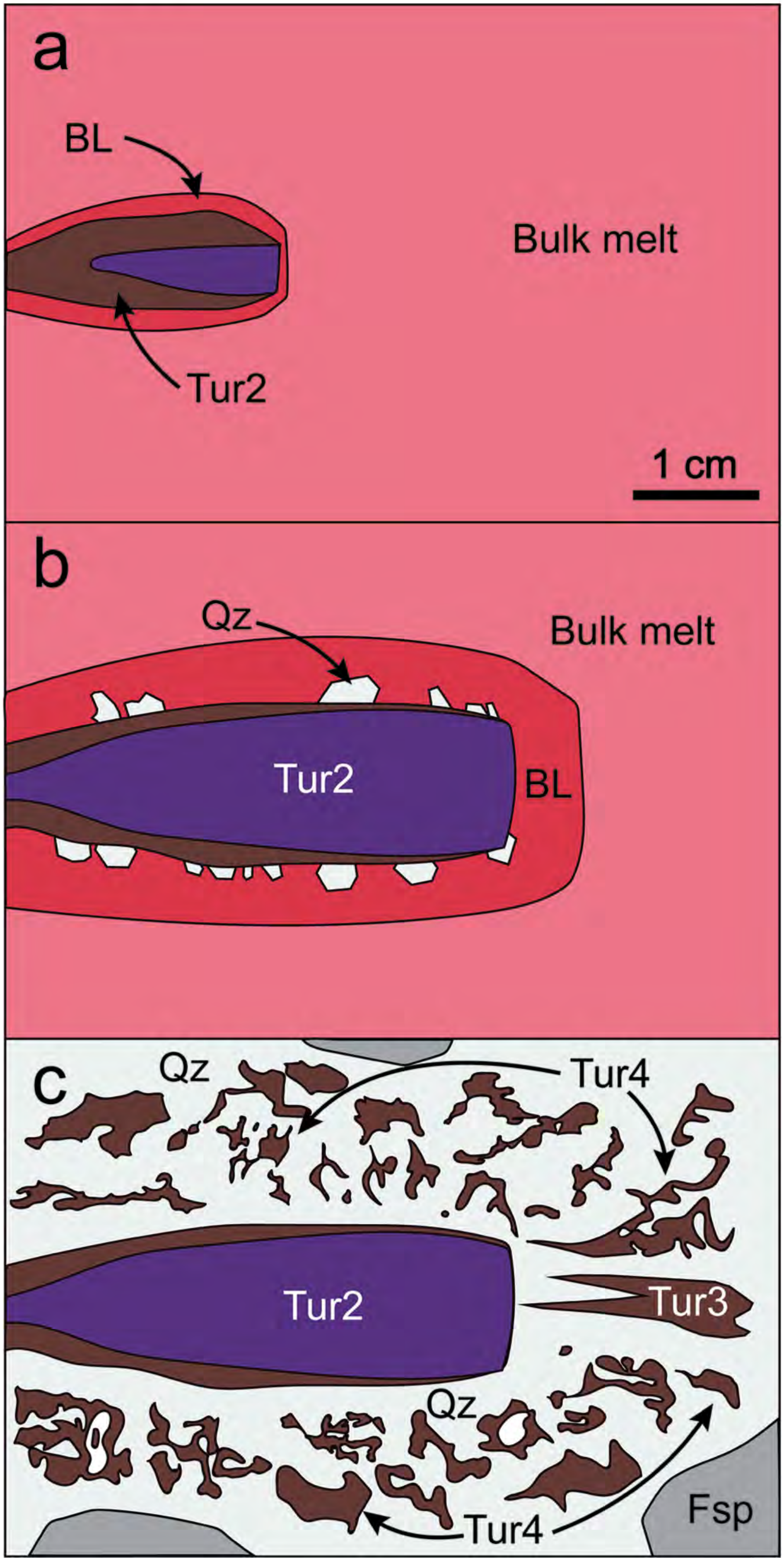
a
BL
Bulk melt
Tur2
1 cm
b
Qz
Bulk melt
Tur2
BL
c
Qz
Tur4
Tur3
Tur2
Qz
Fsp
Tur4

Figure 12

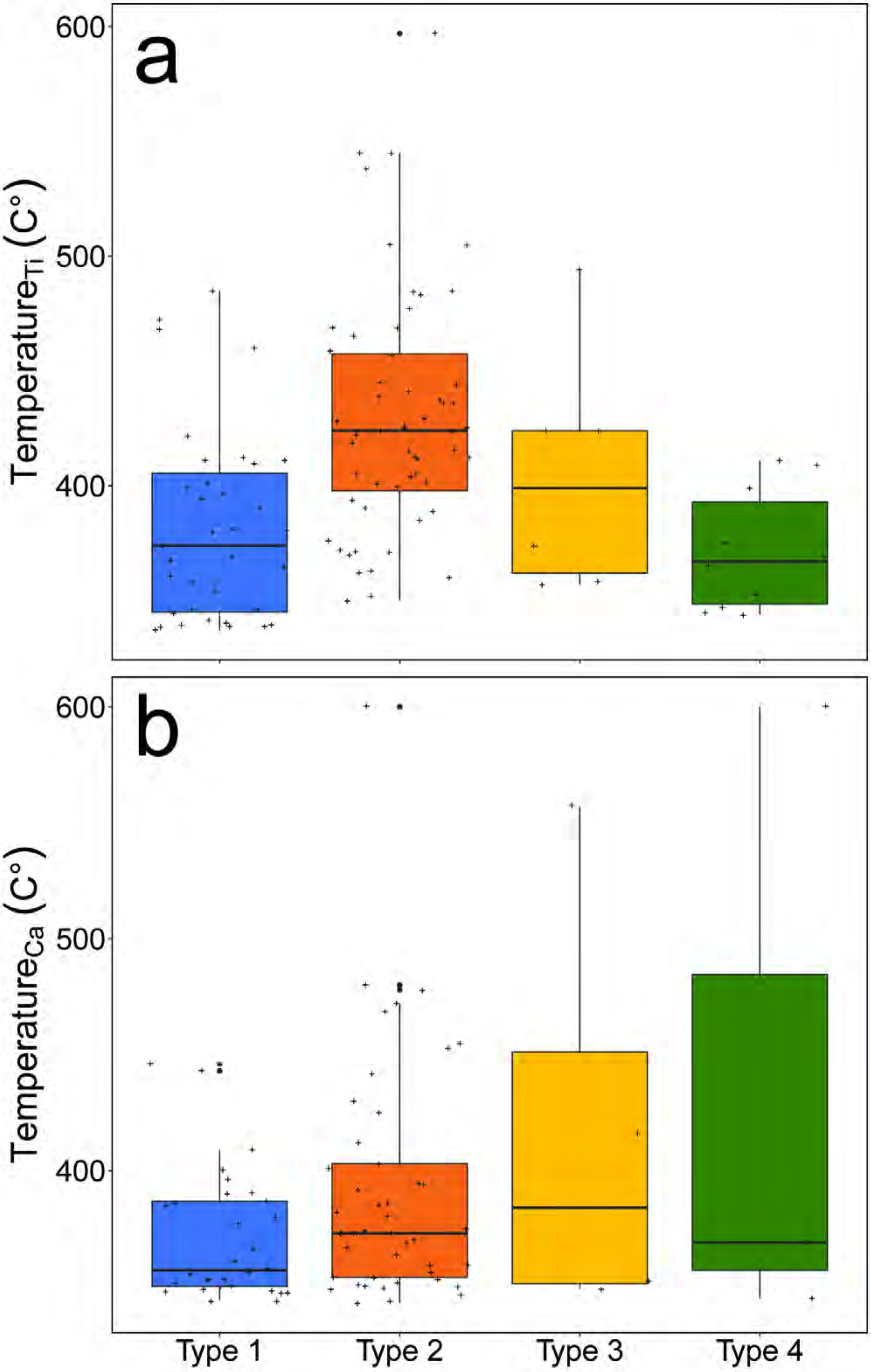
a
600
500
400
Temperature$_{Ti}$ (C°)
b
600
500
400
Temperature$_{Ca}$ (C°)
Type 1
Type 2
Type 3
Type 4